Coastal Engineering 202 (2025) 104847

Contents lists available at ScienceDirect

Coastal Engineering

journal homepage: www.elsevier.com/locate/coastaleng

Breaking occurrence and dissipation in shortcrested waves in finite water

Umniya Al Khalili, Ioannis Karmpadakis *

Department of Civil & Environmental Engineering, Imperial College London, London, SW7 2AZ, UK

A R T I C L E I N F O

Keywords:
Wave breaking
Nonlinear amplification
Energy dissipation
Crest heights

A B S T R A C T

The understanding of wave breaking has long been a critical concern for engineers and scientists. However, accurately identifying the onset of breaking and quantifying the associated energy dissipation remain significant challenges. To address this, the present study develops a novel methodology to identify breaking wave events in shortcrested seas in finite water depths. This is achieved through a unique dataset which couples laboratory and numerically-generated waves. The data reflect realistic sea-states used in engineering design and cover a wide range of conditions from mild to extreme. Using the proposed algorithm, key physical properties of breaking waves are examined. In particular, the probability of wave breaking and the associated wave energy dissipation are quantified to provide a statistical description of their behaviour. Complementarily, waves exhibiting significant nonlinear amplifications are also identified and modelled in a similar manner. This enables traditional wave distributions to be decomposed into more detailed distributions of breaking and non-breaking waves. These insights are combined to define a new model that predicts crest height statistics in intermediate water depths. This new mixture model is shown to reproduce experimental measurements with high accuracy, while also providing critical additional information about wave breaking.

1. Introduction

The behaviour of real ocean waves is highly complex. As waves propagate in coastal regions, they experience nonlinear interactions which amplify the wave field (Tayfun, 1980; Fedele and Tayfun, 2009). This results in a steepening of the waves and an overall increase in their instability. When this steepening cannot be sustained further, some of the wave energy is transformed into kinetic energy and turbulence (Dean and Dalrymple, 1991). This process is referred to as wave breaking. In analysing breaking waves, it is important to not only establish a condition to define when waves break but also how their properties change during the breaking process. This is because wave breaking presents important implications across a range of disciplines.

In the context of wave hydrodynamics, the interplay between the effects of nonlinear amplifications and wave breaking define the maximum height of waves (Karmpadakis and Swan, 2022). Moreover, as waves break, they introduce radiation stress gradients. This results in mean water level changes (Longuet-Higgins and Stewart, 1964), the generation of longshore currents (Longuet-Higgins, 1970) and the formation of rip currents (Bowen, 1969).

These mean water level changes are critical to assessing coastal hazards. The increase in the mean water level in the surf zone alongside the more turbulent flow conditions in this region can present notable flooding risk to coastal areas (Raby, 2003). Furthermore, Franco et al. (1995) and Pullen et al. (2009) explain that the more extreme wave conditions associated with breaking events can result in significant overtopping of coastal infrastructure. Hence, understanding these mechanisms is fundamental to the design of coastal defences.

Currents generated during wave breaking play a fundamental role in driving coastal sediment transport (Beach and Sternberg, 1996). In the long-shore direction, oblique wave breaking results in an amplification of local sediment transport rates (Kobayashi et al., 2007). Similarly, in the cross-shore direction, this has implications on beach erosion (Kobayashi and Lawrence, 2004) and sandbar migration (Elsayed et al., 2022). Sandbars act to dissipate wave energy and reduce overtopping rates during storm events (van der Meer et al., 2018). Thus, their migration can expose coastal areas to additional risks.

In the study of wave-structure interaction, wave breaking plays a critical role in both deep and shallow water contexts. In deep water, Ma and Swan (2020) explain that the susceptibility of offshore platforms to wave-in-deck loading (WID) is heightened during a breaking event. Furthermore, the introduction of breaking effects can significantly alter the response of a floating body (Faltinsen, 1990). In shallow water, Cuomo et al. (2010) outlines additional slamming force contributions from breaking waves on seawalls. This refers to a localised high-pressure dynamic force contribution which presents significant threat to coastal

* Corresponding author.
E-mail addresses: umniya.al-khalili18@imperial.ac.uk (U. Al Khalili), i.karmpadakis@imperial.ac.uk (I. Karmpadakis).

https://doi.org/10.1016/j.coastaleng.2025.104847
Received 15 April 2025; Received in revised form 29 July 2025; Accepted 29 July 2025
Available online 6 August 2025

infrastructure (Stansberg et al., 2012). The importance of wave breaking also extends to establishing the survivability of both marine renewables (Faltinsen et al., 2004) and offshore wind platforms (Stansby et al., 2013).

Wave breaking also has a substantial environmental impact (Deane et al., 2016a,b). The generation of turbulence during the breaking process enhances mass and momentum transport across the air-sea interface (Drazen et al., 2008; Schwendeman et al., 2014). This mechanism controls the extent of gas exchange in this region (Keeling, 1993), resulting in a reduction in the rate of CO_2 released to the atmosphere. Instead, the entrainment of CO_2 by the water causes ocean acidification, which has significant ramifications on marine life (Deike et al., 2016). In addition, the spray generated during wave breaking is transported to the atmosphere. Andreas et al. (1995) explain that this has consequences in altering the atmospheric chemistry, cloud formation, heat and moisture exchange. Thus, the consideration of these effects is pertinent to both local and global climate scales.

Understanding the occurrence of wave breaking and the effects associated with breaking waves are two key questions in coastal and ocean engineering applications. Despite many advances in the literature, there still remain several open questions regarding the occurrence of wave breaking and particularly its implications (Babanin, 2011). To address these, the present work utilises long, random experimental records of short-crested waves in intermediate water depths to define a novel methodology that classifies breaking and non-breaking waves. This is achieved by conducting potential flow numerical simulations using the same conditions as the experiments and improving a method originally proposed by Karmpadakis and Swan (2020). The fusion between experimental and numerically-simulated waves allows for an accurate wave-by-wave analysis and classification within sea-states of interest. These results are used to produce robust estimations of (a) the probability of wave breaking, and (b) the associated wave energy dissipation. Importantly, these findings are used to develop a statistical mixture model that is able to accurately capture extreme crest height statistics in intermediate water.

2. Background

2.1. Theoretical wave modelling

Considering linear random wave theory (LRWT) (Airy, 1845), the water surface elevation correct to first order, $\eta^{(1)}(\mathbf{x}, t)$, is given by:

$$\eta^{(1)}(\mathbf{x}, t) = \sum_{i=1}^{\infty} a_i \cos\left(\mathbf{k_i x} - \omega_i t + \phi_i\right), \tag{1}$$

where $\mathbf{x} = (x, y)$ are the horizontal coordinates, t is the time vector, i denotes an individual wave harmonic with amplitude a_i, wave number $\mathbf{k_i} = (k_x, k_y) = (k\cos\theta_i, k\sin\theta_i)$, angular frequency ω_i, direction θ_i and initial phase ϕ_i.

Although Eq. (1) provides an initial linear approximation to the water surface elevation, real seas exhibit nonlinear properties, particularly in more extreme cases (Guedes Soares and Pascoal, 2005). Longuet-Higgins and Stewart (1960) and Sharma and Dean (1981) extended the description of random waves to second-order by appending an additional second-order bound contribution to the linear approximation (Eq. (1)). This second-order contribution consists of frequency-difference terms, $\eta^{(2-)}$, and frequency-sum terms, $\eta^{(2+)}$, expressed as:

$$\eta^{(2-)}(\mathbf{x}, t) = \sum_{i=1}^{\infty}\sum_{j=1}^{\infty} M^{ij-} \cos\left(\Psi_i - \Psi_j\right), \tag{2}$$

$$\eta^{(2+)}(\mathbf{x}, t) = \sum_{i=1}^{\infty}\sum_{j=1}^{\infty} M^{ij+} \cos\left(\Psi_i + \Psi_j\right), \tag{3}$$

where M^{ij-} and M^{ij+} are the interaction kernels given in Sharma and Dean (1981) and $\Psi = (\mathbf{kx} - \omega t + \phi)$ for each (i, j) wave harmonic. The frequency-difference terms are low frequency contributions (also referred to as group terms), whilst the frequency-sum terms denote high-frequency oscillations. Utilising these formulations, the total surface elevation as denoted by second-order random wave theory (SORWT) is:

$$\eta^{(2)} = \eta^{(1)} + \eta^{(2-)} + \eta^{(2+)}. \tag{4}$$

2.2. Crest height distributions

Although SORWT simulations provide a full description of the sea-state correct to second-order of wave steepness, in practical applications, the simplicity of crest height distribution is preferred. Given the importance of accurately modelling the short-term wave statistics in design, a plethora of crest height distributions have been proposed in literature.

The Rayleigh crest height distribution (Longuet-Higgins, 1952) assumes a linear narrow-banded sea-state, idealised by considering no wave breaking. The functional form of the model is given by:

$$Q(\eta > \eta_c) = \exp\left[-\frac{1}{\alpha}\left(\frac{\eta_c}{H_s}\right)^{\beta}\right], \tag{5}$$

where η_c is the crest height, $\alpha = \frac{1}{8}$ is the scale parameter and $\beta = 2$ is the shape parameter. The Rayleigh formulation is known to significantly under-estimate crest heights occurring at small probabilities of exceedance as a result of its linear assumption (Tayfun, 1981; Prevosto et al., 2000). To overcome these limitations, Tayfun (1980) derived an analytical model to describe the crest height distribution which includes effects arising at a second-order of wave steepness with an underlying narrow-banded spectrum. Effects arising at second-order were also considered by Forristall (2000) that proposed a crest height distribution based on an empirical fit to second-order random wave simulations of realistic ocean spectra. The Forristall (2000) model is often the chosen short-term crest height distribution adopted in design practice (Det Norske Veritas, 2010) and has historically been the basis for offshore and coastal structures design. This formulation allows for the effects of wave steepness and reduced effective water depth to be captured. The functional form of the model is as given by Eq. (5); however, unlike the Rayleigh model, α and β are no longer constants. Their value is dependent on the steepness parameter (S_1), which characterises the degree of nonlinearity of waves, and the Ursell number (U_r), which characterises the influence of the effective water depth on wave nonlinearity. The expressions for α and β for short-crested seas are based on Forristall's Weibull fit to short-crested simulations which give:

$$\begin{aligned} \alpha &= \frac{1}{2\sqrt{2}} + 0.2568 S_1 + 0.0800 U_r, \\ \beta &= 2 - 1.7912 S_1 - 0.5302 U_r + 0.2840 U_r^2, \end{aligned} \tag{6}$$

where $S_1 = \frac{2\pi H_s}{g T_1^2}$, $U_r = \frac{H_s}{k_1^2 d^3}$ and k_1 is the wavenumber corresponding to the mean wave period, T_1.

Considerations of effects occurring at third-order of wave steepness were described by Tayfun and Fedele (2007), who derived a model based on a Gram–Charlier series expansion. In assessing these models, particularly in the context of extreme waves, the key aspect is their ability to capture the competing effects of higher-order nonlinearities and wave breaking. Latheef and Swan (2013) and Karmpadakis et al. (2019) have shown the importance of these competing mechanisms for the validity of crest height distributions, particularly in the context of intermediate water depths. However, a key property neglected by the aforementioned distributions is wave breaking. Karmpadakis and Swan (2022) bridge this gap by proposing a new crest height model based on an extensive database of experimental and field measurements. This model has the following form:

$$\zeta = \frac{\eta_c}{H_s} = \left(\chi + 2\mu\chi^2 + \kappa\mu\chi\right)\cdot\left(A\chi + B\right), \tag{7}$$

where $\chi = \eta_c^{(1)}/H_s$ is the normalised Rayleigh-predicted crest height and μ is a steepness parameter used to incorporate nonlinear effects (Tayfun, 2006). These include effects at second-order ($2\mu\chi^2$) and beyond ($\kappa\mu\chi$), using an additional sigmoid function (κ) defined as:

$$\kappa = \frac{1}{1 + k^3 \exp(-10k\mu)}, \tag{8}$$

where $k = 25.3$ and μ is defined as:

$$\mu = 16\frac{\alpha^3}{\beta}\Gamma\left(\frac{3}{\beta}\right) - \frac{1}{4}\sqrt{\frac{\pi}{2}}, \tag{9}$$

where Γ is the complete gamma function. While the first term of Eq. (7) is shown to capture fully nonlinear crest heights arising through a potential flow assumption, the second term introduces wave breaking. The parameterisation of the breaking function is:

$$A = \begin{cases} -8.46S_1 + 0.9239U_r^2 - 1.742U_r + 0.5148 & \text{for } \mu > 0.065 \\ 0 & \text{otherwise} \end{cases} \tag{10}$$

and

$$B = \begin{cases} -0.4273\mu + 1.203 & \text{for } \mu \geq 0.16 \\ 2.407\mu + 0.8164 & \text{for } 0.065 < \mu < 0.16 \\ 1 & \text{otherwise.} \end{cases} \tag{11}$$

Through a semi-empirical calibration to extensive laboratory measurements, the Karmpadakis and Swan (2022) model has been shown to perform very well across a range of cases in both the laboratory and the field.

2.3. Wave breaking

Given the importance of wave breaking, there is a vast array of studies that describe the evolution of irregular wave fields following breaking initiation in coastal waters. The first aspect to address is how to identify breaking initiation. The methods proposed in literature can be categorised into three types of criteria: geometric, dynamic and kinematic. Traditionally, geometric criteria, which are based on local (Miche, 1944; McAllister et al., 2023) or global (Rapp and Melville, 1990) wave steepness measures, have been used. In coastal waters, Munk (1949) proposed an alternative depth-induced geometric criterion that includes the role of the local water depth. Goda (2000) later established the dependence of this breaking criterion on the beach slope and incident wave steepness. Alternatively, several dynamic criteria for breaking initiation have been put forth. These consider the acceleration of the crest (Longuet-Higgins, 1969), momentum and energy growth rate (Banner and Tian, 1998) and higher harmonic energy evolution (Rapp and Melville, 1990; Kway et al., 1998). However, the application of these methods in practice is generally limited. Instead, the kinematic criterion is often implemented, based on the particle and phase velocities. Most notably, the criteria of Barthelemy et al. (2018) defines breaking onset based on the ratio of the horizontal velocity to the wave celerity. This condition has been broadly validated (e.g. Derakhti et al., 2020) and implemented in numerical models (Seiffert et al., 2017; Benoit et al., 2024). Wu and Nepf (2002) explain that the kinematic criterion is the most robust, particularly in the context of directional seas.

In the field, breaking detection historically was based on visual detection methods which utilised white-cap coverage as a metric to identify breaking waves from sea surface photographs. This evolved to utilise sea surface mapping instrumentation to identify breakers through fluctuations in the surface elevation measurements (Weissman et al., 1984; Holthuijsen and Herbers, 1986). In tandem with the developments in instrumentation in physical oceanography, new instrumental detection methods have emerged. This involves passing data such as surface elevation, velocity, acceleration and volume of air entrapment through a detection filter (Tucker and Pitt, 2001). The variance in the surface elevation (Martins et al., 2017), the unevenness of the sea surface (Jessup et al., 1997; Zappa et al., 2001; Sutherland and Melville, 2013) and the water void fraction (Su and Cartmill, 1991; Lamarre and Melville, 1994; Gemmrich and Farmer, 1999) may be used as a proxy for wave breaking. More recently, technological advancements have given rise to automated algorithms which detect individual wave breakers (Melville and Matusov, 2002; Gemmrich et al., 2008). The most promising alternative to these methods is proposed by Liberzon et al. (2019). They utilise the signal processing techniques of Huang et al. (1992) and Stansell and MacFarlane (2002) to identify wave breaking from the timeseries of the water surface elevation.

The challenge in charachterising wave breaking in irregular seas lies in the quantification of the breaking probabilities within a sea-state. Banner et al. (2000) related the probability of breaking to a threshold describing the nonlinearity of the waves. They explain that once this breaking threshold is reached, the breaking probability depends quadratically on the significant wave steepness. Likewise, Babanin et al. (2001) identified a threshold-like behaviour of breaking probabilities across the spectrum in terms of spectral steepness parameters. A similar threshold was described by Banner et al. (2002) based on a spectral measure of the wave steepness, referred to as the spectral saturation. Their analysis confirmed the strong correlation between the probability of breaking and the mean spectral saturation. More recently, the work of Filipot et al. (2010) developed a unified deep-to-shallow water wave-breaking probability parameterisation.

Alongside defining the breaking probability, it is important to quantify the breaking energy dissipation. Early work by Le Méhauté (1962) stated that the dissipation rate of a breaking wave is analogous to a tidal bore, thus adopting a quasi-uniform wave approximation. Utilising this concept, Battjes and Janssen (1978) catalysed the development of the parametric approach by quantifying the dissipation rate per breaking wave and providing an expression for the probability of occurrence of breaking waves utilising a truncated Rayleigh probability distribution of the wave heights. Thornton and Guza (1983) adopted a similar concept with a modified bore model. Other similar approaches to define the wave height distribution in the surf zone were presented by Battjes and Stive (1985), Baldock et al. (1998) and Alsina and Baldock (2007).

Considering numerical simulations, Computational Fluid Dynamics (CFD) may be employed to produce high fidelity simulations of breaking waves (Li et al., 2022). There exist several models in the literature that can be used for this purpose. Notable examples include OpenFOAM (e.g. Higuera et al., 2013; Hu et al., 2016), Basilisk (e.g. Mostert et al., 2022; Liu et al., 2023) and SPH (e.g. Dalrymple and Rogers, 2006; Altomare et al., 2023). Despite the fact that these models are able to provide accurate results, their significant computational cost means they cannot feasibly be used to determine wave statistics. Alternatively, lower fidelity models derived on the assumption of potential flow can be used alongside parametrisations for wave breaking. For example, established potential flow models used in this capacity include OceanWave3D (Engsig-Karup et al., 2009), REEF3D (Bihs et al., 2016) and the High Order Spectral (HOS) models HOS-ocean/HOS-NWT (Ducrozet et al., 2012, 2016). The direct use of these models in the simulation of a steep wave field leads to instabilities and eventually termination of simulations (Spiliotopoulos and Katsardi, 2024). The inclusion of methods to parameterise breaking effects seeks to overcome these limitations. Tang et al. (2023) apply low-pass filtering of the energy spectra in OceanWave3D to account for breaking effects. For long-crested waves, Seiffert et al. (2017) and Seiffert and Ducrozet (2018) have introduced the breaking criteria of Barthelemy et al. (2018) and a source dissipation term (Tian et al., 2012) to include breaking effects. This approach has shown good results for unidirectional waves (Craciunescu and Christou, 2020) as long as only weak breakers are present, as well as the potential to be applied to long random simulations. However, direct application of this approach to short-crested waves is challenging due to the lack of an efficient methodology to track wave crests (Wang and Ducrozet, 2025). This has important implications on

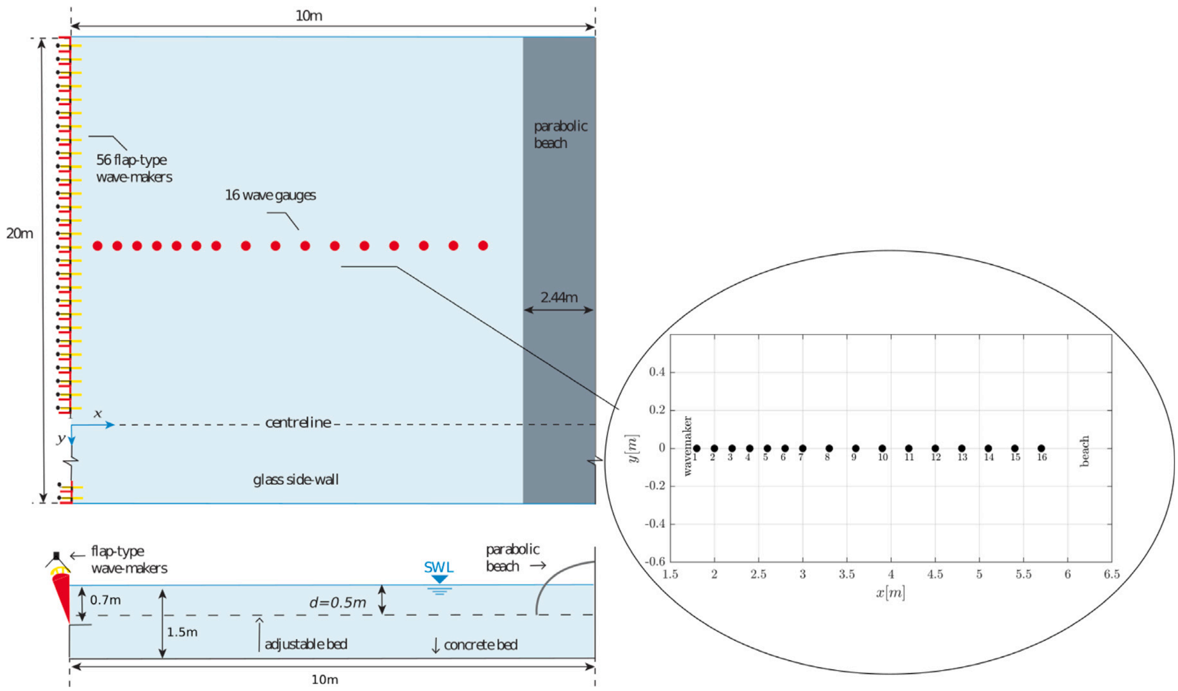

Fig. 1. Experimental set-up in Imperial College London wave basin.

defining the local wave crest phase speed, on which thresholds such as the Barthelemy et al. (2018) criteria depend on.

This shortcoming provides a strong motivation for the present work. The proposed method to identify the occurrence of wave breaking and associated dissipation can provide guidance for the development of appropriate numerical formulations relevant to short-crested seas. Similarly, alternative models that already include parametrised breaking terms, such as SWASH (Zijlema et al., 2011) and FUNWAVE (Shi et al., 2012) can use these results to verify their applicability.

3. Methodology

3.1. Experimental wave generation and validation

The experimental data, which forms the basis of the analysis in this study, was generated by Karmpadakis (2019) in the Imperial College London wave basin, with plan dimensions $10\,\text{m} \times 20\,\text{m}$ and a water depth $d = 0.5\,\text{m}$. The basin contains 56 bottom-hinged, flap-type wave paddles, as illustrated in Fig. 1. Wave generation and active wave absorption were based on force-feedback control in conjunction with efficient passive absorption beaches downstream (Karmpadakis et al., 2019). In doing so, the magnitude of the reflection coefficient was ensured to be of the order of 5%, indicating the relatively negligible effects of wave reflection. Measurements of the water surface elevation were made using 16 resistive wave gauges located along the centre-line of the wave basin as shown in Fig. 1. Each wave gauge is sampling at a rate of $f_s = 128\,\text{Hz}$, which is sufficient to resolve high-frequency effects and avoid the requirement for additional post-processing. Further details of the experimental method and validation of the facility are provided by Masterton and Swan (2008), Spinneken and Swan (2012), Latheef et al. (2017) and Karmpadakis et al. (2019). Karmpadakis (2019) has demonstrated consistency between the measured data in various facilities with varying basin dimensions, wave generation mechanisms and energy absorption strategies and validated experimental results against field data. The agreement across this extensive dataset demonstrates the accuracy of the experimentally-generated sea-states to represent real seas in intermediate waters.

The generated sea-states are all random and directionally-spread in nature. The chosen sea-states intend to reflect realistic field conditions. As such, the spectral description based on the Joint North Sea Wave Project (JONSWAP) (Hasselmann et al., 1973) is adopted. The spectral density function of this formulation is given as:

$$S_{\eta\eta}(\omega) = \frac{\alpha g^2}{\omega^5} \exp\left(\frac{-\beta\omega_p^4}{\omega^4}\right) \gamma^{\exp\left[-\frac{(\omega-\omega_p)^2}{2\sigma^2\omega_p^2}\right]}, \tag{12}$$

where ω_p is the circular wave frequency corresponding to the spectral peak, $\beta = 1.25$, $\sigma = 0.07$ for $\omega \le \omega_p$ and $\sigma = 0.09$ for $\omega > \omega_p$. The peak enhancement factor, γ, is set to 2.5 to reflect realistic sea-states in intermediate water (Jonathan and Taylor, 1997).

To generate directionally-spread seas, a wrapped normal frequency-independent directional spreading function (DSF), $D(\theta)$, is utilised given by:

$$D(\theta) = \frac{A}{\sigma_\theta} \exp\left(-\frac{\theta^2}{2\sigma_\theta^2}\right), \tag{13}$$

where σ_θ is the standard deviation of the normal directional spreading and A is the normalising factor such that $\int_0^{2\pi} D(\theta)d\theta = 1$. Utilising the JONSWAP spectra given by Eq. (12) in conjunction with the DSF given by Eq. (13), the directionally-spread spectrum is defined as:

$$F(\omega, \theta) = S_{\eta\eta}(\omega) D(\theta). \tag{14}$$

Each wave component is assigned a direction of propagation that is randomly selected from the DSF. This method, known as the Random Directional Method (RDM), ensures that each frequency component is generated in only one direction. Latheef et al. (2017) has shown the suitability of this method relative to other methods such as the double and single summation. More specifically, it is able to achieve accurate and ergodic short-crested seas whilst adopting a realistic frequency resolution.

The target sea-states investigated are defined by 3 variables: (H_s, T_p, σ_θ), where H_s is the significant wave height and T_p is the peak spectral period. A summary of the experimental test cases is provided in Table 1. The experimentally-generated sea-states adopt a Froude similarity scaling to field scale such that the length scale is l_s = 1:100 and corresponding time scale is t_s = 1:10. Heller (2017) has outlined

Table 1
Experimental test cases.

Sea-state	T_p [s]	H_s [mm]	S_p [–]	$\frac{H_s k_p}{2}$ [–]	σ_θ [°]	$k_p d$ [–]
A1		22	0.01	0.035		
A2		44	0.02	0.069		
A3		67	0.03	0.103		
A4	1.2	89	0.04	0.138	10,20	1.53
A5		112	0.05	0.172		
A6		134	0.06	0.207		
A7		157	0.07	0.241		
B1		30	0.01	0.037		
B2		61	0.02	0.075		
B3		91	0.03	0.112		
B4	1.4	122	0.04	0.150	10,20	1.22
B5		153	0.05	0.187		
B6		183	0.06	0.224		
C1		39	0.01	0.040		
C2		79	0.02	0.081		
C3	1.6	119	0.03	0.122	10,20	1.02
C4		159	0.04	0.163		
C5		199	0.05	0.204		

the importance of adopting appropriate scaling in laboratory investigations to minimise scale effects. His work has shown the effectiveness of Froude scaling in hydraulic modelling of free surface flows.

The sea-states in Table 1 consist of 3 sets of sea-states with the same peak period, T_p, and hence, propagating over the same effective water depth, $k_p d$, where k_p is the wave number associated with the peak period, T_p. Within each set of sea-states, the sea-state steepness, S_p, defined as:

$$S_p = \frac{2\pi H_s}{g{T_p}^2}, \tag{15}$$

is varied. In total, between 5–7 steepness cases are generated for each set. In addition, for each sea-state, the experimental data is generated using 20 random simulations (seeds) with equivalent inputs of amplitude, frequency and direction of propagation. Each seed has a duration of 1024 s, which is approximately 3 h in field scale. Hence, the target spectrum has a resolution of $\Delta f = 1/1024$ Hz, which is used as an input to the wavemaker. Based on this methodology, each seed consists of 2145 individual wave components which are assigned an initial phase, ϕ, which is randomly distributed between $[0, 2\pi]$. This method is referred to as the deterministic amplitude approach since the adopted target spectrum allows for the amplitude of each wave to be defined explicitly (Karmpadakis and Swan, 2020). Grigoriu (1993) has demonstrated the effectiveness of this method at exhibiting stronger ergodic properties relative to the random amplitude approach. The deterministic amplitude approach ensures the amplitude spectrum is the same for each seed and its magnitude is only scaled linearly with increasing sea-state steepness, as illustrated in Fig. 2(a). This ensures that the additional nonlinearity associated with the relative phasing of the interacting wave components is explicitly defined.

Another fundamental aspect to note is the initial phases for sea-states of increasing steepness. For a seed of the same peak period, T_p, and directional spread, σ_θ, the phases and directions assigned to each seed remain constant. In doing so, a deterministic comparison between test cases of increasing steepness but the same T_p and σ_θ can be made since the only variability is the scaling of the amplitude spectrum. This is shown in Fig. 2(b) such that the phasing of the surface elevations measured across sea-states of increasing steepness, S_p, is equivalent. As a whole, the large number of waves modelled using this methodology allows sea-states with small probabilities of exceedance that have not been observed in the field but are generated experimentally, to be analysed, which is of particular interest in design.

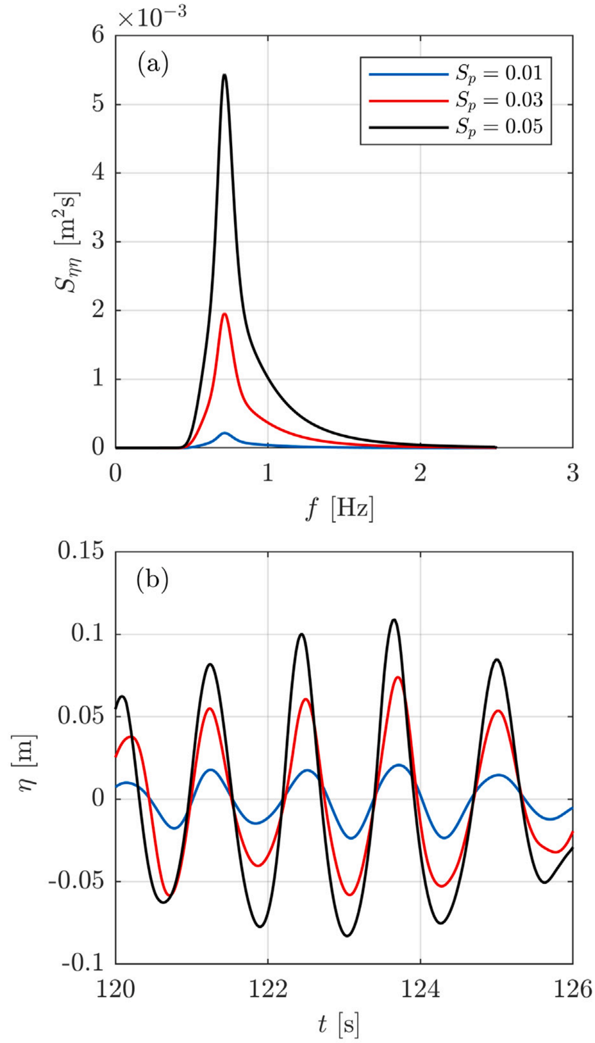

Fig. 2. (a) Energy spectra and (b) time series of the water surface elevation for $\sigma_\theta = 10°$, $k_p d = 1.22$. The colour of the line corresponds to the sea-state steepness, S_p.

3.2. Numerical simulations

In addition to the experimental data, simulations are conducted based on SORWT (Eq. (4)) for equivalent sea-states to the laboratory test cases and using the same input conditions and output locations. This methodology allows for direct comparison between the second-order simulations and the laboratory data. The use of SORWT has the advantage of providing computationally-fast simulations to second-order accuracy.

Fig. 3 presents a segment of the time series of the water surface elevation for $\sigma_\theta = 10°$, $k_p d = 1.22$ with increasing sea-state steepness, S_p. The time vector has been adjusted such that the location of the crest at the first steepness, $S_p = 0.01$, is at $t = 0$ s. Due to the phase alignment for sea-states of increasing steepness, the superposition of the corresponding time series, both experimentally and numerically, allow for a direct comparison of equivalent waves across sea-states of varying steepness.

If we begin by analysing the shape of the numerical waves shown in Fig. 3(a), it is evident that with increasing steepness, the extent of the vertical asymmetry, caused by the presence of second order bound wave contributions, increases. This is observed as sharper crests and shallower troughs. However, the wave profiles show no evidence of

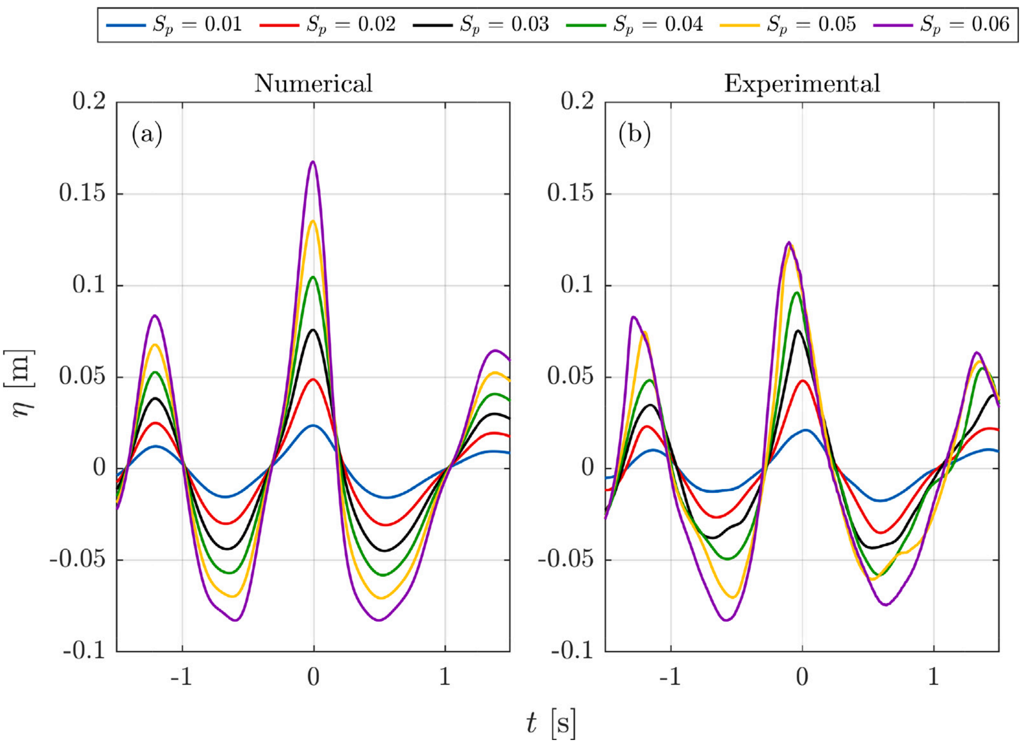

Fig. 3. Time series of the water surface elevation for $\sigma_\theta = 10°$, $k_p d = 1.22$ for the (a) numerical and (b) experimental dataset. The colour of the line corresponds to the sea-state steepness, S_p.

horizontal asymmetry. Conversely in the experimental dataset shown in Fig. 3(b), both vertical and horizontal asymmetry is observed where waves in the experiment are shown to tilt towards the front as they are amplified resulting in an increasing positive skewness of the surface elevation (Longuet-Higgins, 1982). This has previously been explained by Karmpadakis and Swan (2020). Another notable distinction experimentally is that the crest height for $S_p = 0.06$ is comparable to that of $S_p = 0.05$. This is because, experimentally, highly asymmetric and steep waves undergo energy dissipation to stabilise, resulting in wave breaking. This demonstrates the limiting effect of wave breaking on crest statistics, which is not considered numerically.

These effects are further highlighted by Fig. 4 which superimposes numerically-simulated time series (dashed lines) on to experimental time series (solid lines) for $\sigma_\theta = 10°$, $k_p d = 1.22$ and increasing sea-state steepness. The agreement in space and time between numerical simulations and the experiments indicates the lack of spurious waves or significant reflection in the wave field (Karmpadakis and Swan, 2020). In comparing the relative magnitude of the crest height experimentally and numerically, the results are conditional on the sea-state steepness. In less steep seas, $S_p = 0.01$, there is good correspondence between the experimental and numerical time series, indicating the validity of SORWT in these cases. However, divergence in the results becomes evident in sea-states of moderate steepness, $S_p = 0.03$, such that SORWT is shown to slightly underestimate crest heights in such cases. This demonstrates the importance of nonlinear effects occurring beyond second-order (third-order and above). In highly nonlinear seas, $S_p = 0.05$, the experimental crest height is shown to be less than its SORWT counterpart. This observation, in conjunction with the underestimation of SORWT in moderately steep seas, provides further evidence for the dissipative effect of wave breaking occurring experimentally.

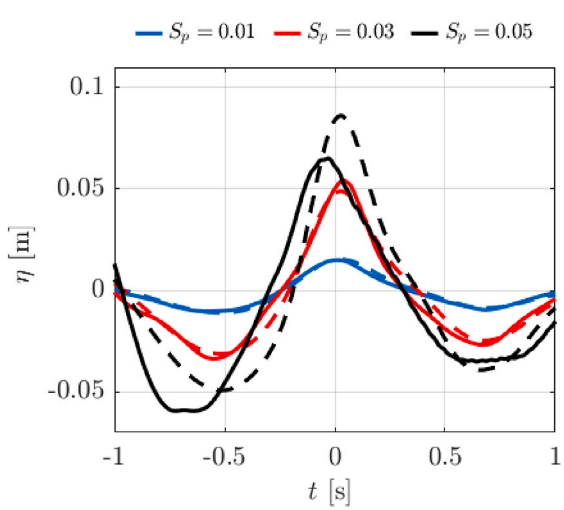

Fig. 4. Time series of the water surface elevation for $\sigma_\theta = 10°$, $k_p d = 1.22$ with experimental and numerical data shown in a solid and dashed line, respectively. The colour of the line corresponds to the sea-state steepness, S_p.

3.3. Wave classification algorithm

A comparison of a given experimentally-measured crest height to the corresponding numerically-simulated crest can provide information on the classification of a particular wave. In other words, if the

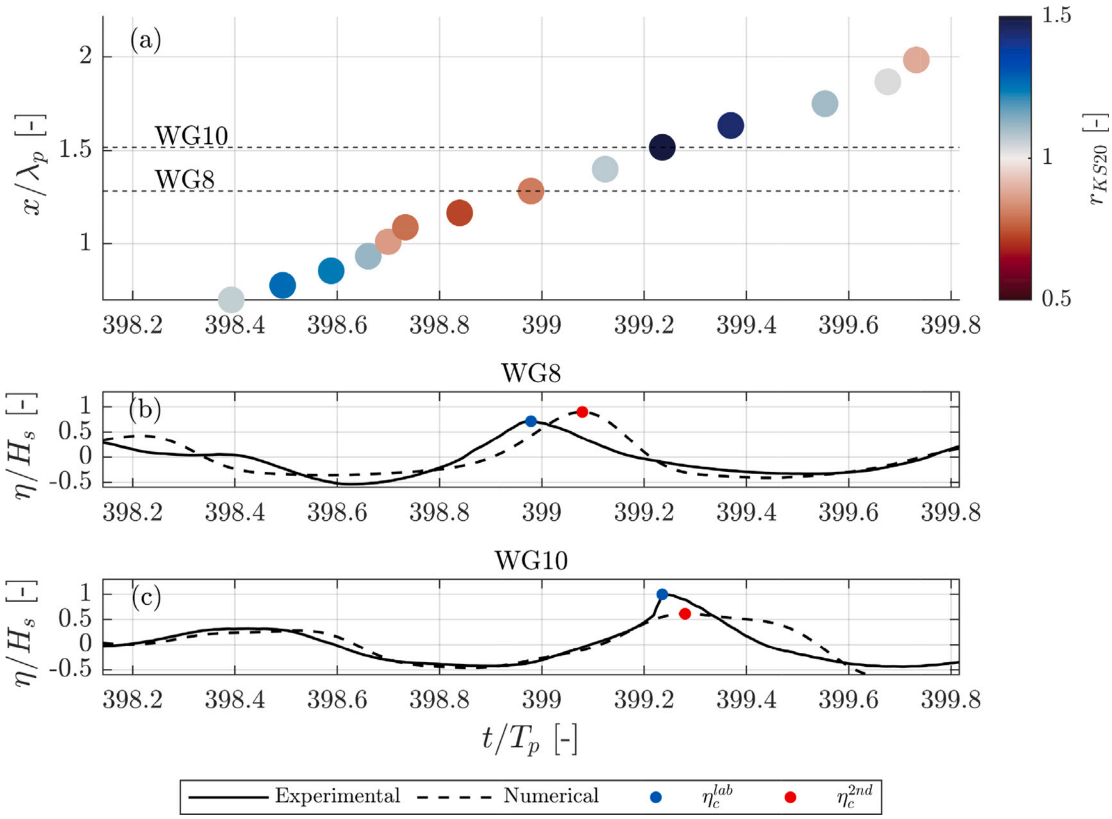

Fig. 5. (a) Evolution of the ratio of experimental to numerical crest height, r, in space for $\sigma_\theta = 10°$, $k_pd = 1.22$, $S_p = 0.04$. Red markers indicate waves are breaking and blue markers indicate waves are amplified relative to second-order theory. Time series of water surface elevation at (b) WG8 and (c) WG10. Experimental and numerical surface elevations are shown in solid and dashed lines, respectively. The experimental and numerical crest height of interest is indicated by a blue and red marker, respectively.

experimental crest height is greater than the numerical counterpart, this indicates the presence of nonlinear effects beyond second-order occurring experimentally. Conversely, a smaller experimental crest indicates the presence of energy dissipation in the form of wave breaking occurring experimentally. Karmpadakis and Swan (2020) utilised this concept to classify individual waves. This involves comparing each experimentally-measured crest, η_c^{lab}, to the corresponding numerically-simulated crest, η_c^{2nd}, such that the ratio of the two indicates whether a given wave is breaking. This ratio is formally defined as:

$$r_{KS20} = \frac{\eta_c^{lab}/H_s^{lab}}{\eta_c^{2nd}/H_s^{2nd}}, \tag{16}$$

such that the crest heights are normalised by their respective significant wave height, H_s, to remove any minor dependencies on this parameter.

A subtle but important aspect to note is the location, in both space and time, at which this classification is computed. The work of Karmpadakis and Swan (2020) based their analysis on results arising at the same spatial location. To assess this method, Fig. 5(a) demonstrates the evolution in the location of an experimental crest in time and space for $\sigma_\theta = 10°$, $k_pd = 1.22$, $S_p = 0.04$. The colour of the marker reflects the ratio of experimental to numerical crest height at each spatial location, r_{KS20}. As such, red colours ($r_{KS20} < 1$) indicate a "broken" wave whereas blue colours ($r_{KS20} > 1$) indicate "amplified" waves. If the waves are classified by considering a single location in space, such as the central location (WG8), then the results of the analysis would indicate that at this location, the wave is "broken". The time series at this location is shown in Fig. 5(b). As evident from this segment of the time series, the experimental crest height is smaller than the corresponding numerical crest height. However, if the same wave is tracked to gauges located further downstream and the time series is re-investigated, contradictory observations arise. This is illustrated in Fig. 5 (c). At WG10, the experimental crest height is now larger than the numerical crest height. As such, at this location, the wave is classified as "amplified" as illustrated in Fig. 5(a). The explanation for such discrepancies is the presence of near-resonant interactions in such highly-nonlinear seas. These interactions act to shift the location of the crest in both space and time such that experimentally, the crests are larger at distances downstream of the location of the equivalent largest second-order simulated crest. Similar observations were made by Barratt et al. (2021) and Huo et al. (2023) in the context of quasi-deterministic focused waves in deep water. Thus, the consideration of these effects is rudimentary to correctly classifying individual waves.

To further analyse the extent of these effects, Fig. 6 demonstrates the spatial evolution of the time history of the water surface elevation for $\sigma_\theta = 10°$, $k_pd = 1.22$, $S_p = 0.04$ for (a) experimental and (b) numerical data. In analysing the spatial evolution of the crest, both numerically and experimentally, an initial steepening of the crest is observed as a consequence of the nonlinear interactions. This results in a spatial maximum crest height denoted by the green markers in Fig. 6(a) and (b), where the spatial maximum experimental, ζ_c^{lab}, and numerical crests, ζ_c^{2nd}, are shown using square and triangular markers, respectively. Following this point in space, the crest height is shown to reduce, highlighting the reduction in the influence of these nonlinearities at these spatial locations along with the initiation of wave breaking occurring experimentally. In addition, if we compare the location of the maximum crest in space experimentally and numerically, we observe that experimentally, the spatial maximum crest occurs further downstream (in x) relative to the corresponding numerical crest height. The work of Donelan et al. (1985) explains that this is a consequence of "amplitude dispersion" which results in an underestimation of wave speed by lower-order solutions compared to laboratory observations.

The effects of amplitude dispersion are further illustrated in Fig. 6(c) which shows the evolution of the surface elevation in space at the time instance of the maximum numerical crest, t_1. We observe that

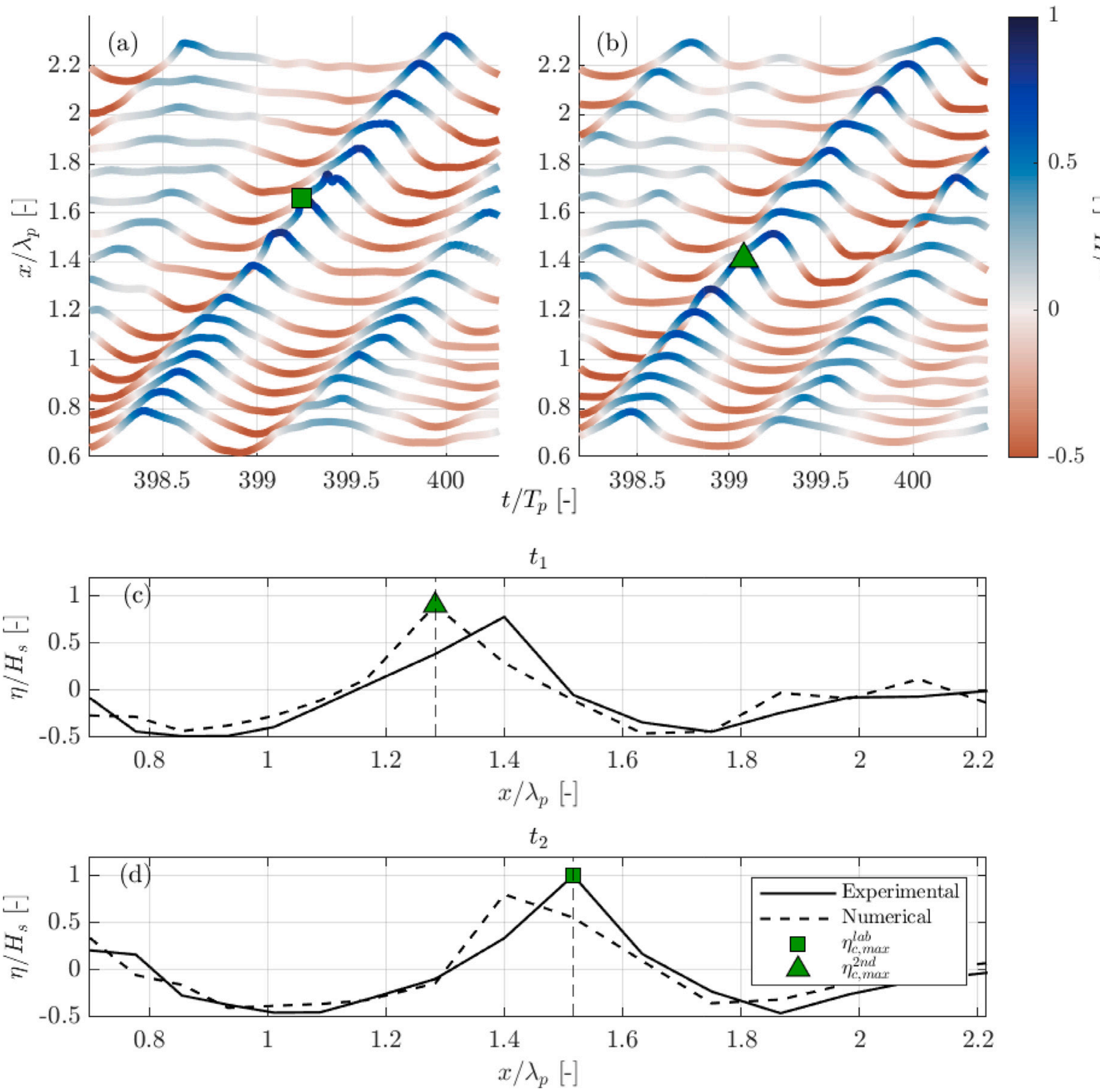

Fig. 6. Spatial evolution of the time history of the water surface elevation for $\sigma_\theta = 10°$, $k_pd = 1.22$, $S_p = 0.04$ for (a) experimental and (b) numerical data. The spatial maximum crest is shown in green square (experimental) and triangular (numerical) markers. Evolution of the water surface elevation in space at the time of the (c) maximum numerical crest height, $t_1 = 558.71$ s, and (d) maximum experimental crest height, $t_2 = 558.93$ s, respectively. Experimental and numerical surface elevations are shown in solid and dashed lines, respectively.

at this instance in time, the magnitude of the numerical crest, shown in a triangular marker, is greater than the corresponding experimental crest. Furthermore, the experimental crest is shown to occur further downstream. However, if we now compare the surface elevations at a later time instance, t_2, as shown in Fig. 6(d), it is observed that the experimental crest height has now increased, resulting in a spatial maximum at a later time and spatial instance, as denoted by the square marker. Hence, experimentally, the largest waves moves to the front of the group as waves propagate spatially (Adcock et al., 2012). Based on the observations made in Fig. 6, it is evident that considering a crest at a single point in time or space is misleading as it does not account for the downshift in the experimental crest.

To quantify the extent of the downshift observed, the parameter $\Delta\hat{x}$ is defined as:

$$\Delta\hat{x} = \frac{\overline{x^{lab} - x^{2\text{nd}}}}{\lambda_p}, \tag{17}$$

where $\overline{x^{lab} - x^{2\text{nd}}}$ is the mean difference in the location of the spatial maximum crest experimentally to that numerically and λ_p is the peak spectral wavelength. The variation in $\Delta\hat{x}$ with the sea-state steepness for the 100 largest waves in a sea-state is shown in Fig. 7 for $\sigma_\theta = 10°$, $k_pd = 1.22$. In addition, the 95% confidence interval, calculated using the bootstrap method (Efron and Tibshirani, 1994), is illustrated using a black dashed line. The findings suggest that the extent of the mean downshift in the spatial maximum crest is greater with increased sea-state steepness. This indicates that for mild seas, SORWT is sufficient and the downshift effect is minimal. However, the relative importance of this effect increases in sea-states of greater steepness. Furthermore, a plateau is observed in the steepest seas such that the mean extent of this downshift is approximately $0.112\lambda_p$. The confidence interval shown indicates a relatively narrow distribution of the parameter $\Delta\hat{x}$ about the mean. However, it is important to note that there are cases where individual waves are observed experimentally at distances as large as $0.5\lambda_p$ downstream of the corresponding numerical crest.

Utilising these findings, the wave classification algorithm proposed is summarised by Fig. 8 considering the classification for a single wave in the fused experimental-numerical dataset. The steps include:

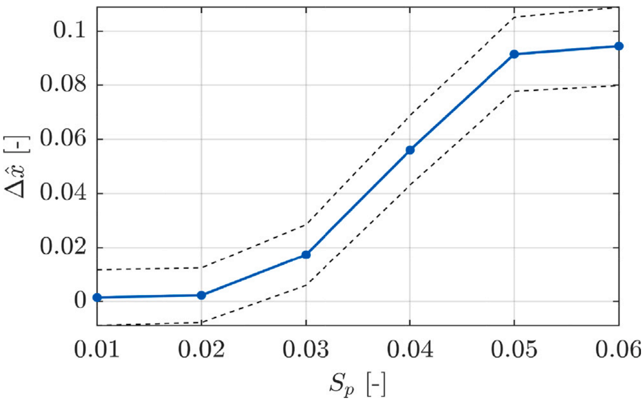

Fig. 7. Variation in $\Delta\hat{x}$ with sea-state steepness, S_p, for the 100 largest waves for $\sigma_\theta = 10°$, $k_p d = 1.22$. The 95% confidence interval is shown in a dashed line.

1. Consider each individual wave at the central gauge, x_0, experimentally ($\eta_c^{lab}{}_{x_0}$) and numerically ($\eta_c^{2\text{nd}}{}_{x_0}$).
2. Define a spatial "window" of width $0.5\lambda_p$, chosen based on the maximum extent of the downshift observed. Track the wave within this spatial window from the central gauge, x_0, to gauges downstream, $x_0 + 0.5\lambda_p$.
3. Define the maximum spatial experimental, ζ_c^{lab}, and numerical, $\zeta_c^{2\text{nd}}$, crest height as the largest value of η_c^{lab} and $\eta_c^{2\text{nd}}$ observed in the spatial window, respectively.
4. Calculate the parameter Δ, defined as the difference in the experimental and numerical crest height normalised by the numerical significant wave height, $H_s^{2\text{nd}}$. This is formally defined by Eq. (18):
$$\Delta = \frac{\zeta_c^{lab} - \zeta_c^{2\text{nd}}}{H_s^{2\text{nd}}}. \tag{18}$$
5. Use the value of Δ to categorise the waves. A value of $\Delta > 0$ indicates that laboratory waves are amplified beyond second-order due to the presence of higher-order nonlinearities. Conversely, a value of $\Delta < 0$ indicates that the laboratory waves have dissipated energy as a consequence of wave breaking. However, to account for minor uncertainties in the measurement of the water surface elevation, a buffer δ is added either side such that three wave populations are defined as:

   (a) $\Delta > \delta$: Wave is amplified
   (b) $-\delta \leq \Delta \leq \delta$: Wave is neither amplified nor breaking
   (c) $\Delta < -\delta$: Wave is broken

For all subsequent analysis, a value of $\delta = 0.10$ is chosen. A discussion on the choice of δ is provided in Appendix A. As a whole, the methodology developed in the present work has no restrictions in generalisability such that the algorithm of wave breaking identification and classification may be applied to any future works utilising a coupled experimental-numerical dataset.

The importance of considering the spatial downshift can be fully realised by the results of this classification. Characteristically, omitting the spatial components and but otherwise following the same method would lead to over predicting the prevalence of wave breaking by up to 30%. To this extent, the probability defined in this work is that of individual waves. This differs from other methods that examine a single point in space.

An important aspect to outline is the use of the parameter Δ to classify waves as opposed to a ratio such as that proposed by r_{KS20}. The ratio r_{KS20} is conditional on the magnitude of the second-order crest height, $\eta_c^{2\text{nd}}/H_s^{2\text{nd}}$. As such, the smallest waves in a given sea-state are biased towards lower values of r_{KS20}. Although this is not significant in steep sea-states where the magnitude of η_c^{lab}/H_s^{lab} negates this, it has highlighted concerns when considering very mild sea-states ($S_p \leq 0.02$). This downward bias results in incorrectly defining very small waves as "broken". Hence, the parameter Δ is alternatively recommended for a more robust classification, which is not biased towards small values of $\eta_c^{2\text{nd}}/H_s^{2\text{nd}}$.

4. Breaking statistics

Utilising the algorithm outlined by Fig. 8, the total population of waves in the dataset can be categorised to produce sub-populations of "broken" and "amplified" waves. In doing so, the statistics of each category of wave can be investigated independently.

4.1. Breaking identification

We will first begin by identifying breaking waves to provide evidence for which waves in a sea-state are most susceptible to breaking. In other words, we seek to answer "which numerically-simulated waves will break experimentally?". This is achieved by utilising the coupled experimental and numerical datasets to conduct a wave-by-wave comparison across the two datasets. Fig. 9 is a scatter plot showing the normalised crest heights, η_c/H_s, plotted against the normalised trough-to-trough wave period, T_{tt}/T_p, for (a) numerical and (b) experimental data for $\sigma_\theta = 10°$, $k_p d = 1.22$, $S_p = 0.05$. The results of this figure suggest that although the scatter of waves across the two datasets may be similar, there are clear discrepancies observed.

Since the largest waves are of interest in design, second-order simulated crest heights are ranked based on their magnitude and the 5 largest waves in the numerical dataset are shown in square markers in Fig. 9(a) alongside the corresponding tracked experimentally-generated crest height in Fig. 9(b). Given the large steepness of the sea-state, this rank is not maintained across datasets such that the largest second-order crest heights are scattered throughout the distribution of experimental data. Experimentally, these crests have broken, thus dissipating a finite amount of energy and reducing in crest height. As such, these waves are experimentally redistributed to larger probabilities of exceedance. Karmpadakis and Swan (2020) have demonstrated that the extent of the redistribution of waves towards larger probabilities of exceedance is more prominent in steeper seas which are more dominated by breaking effects. This redistribution is not observed numerically since SORWT does not include the physical effects of wave energy transfer and wave breaking, which are characteristic of real waves.

Although the presence of wave breaking is well-understood, the extent of its effect on reducing crest heights is not well-documented. Previously, the largest waves were believed to remain in the tail of the distribution so no redistribution across the probabilities of exceedance is observed due to the minimal extent of breaking-induced crest height reduction (Battjes and Groenendijk, 2000). However, it is evident from the coupled dataset presented in this work for a range of sea-states that the influence of wave breaking on the redistribution of crest heights is more significant.

Following the same approach, all numerically-generated waves are mapped to the experimental equivalents and the value of Δ is determined. The contours in Fig. 9 illustrate the variation of Δ in the parameter space for numerical (Fig. 9(a)) and experimental waves (Fig. 9(b)). It is important to note that the results shown in Fig. 9 relate to an extreme sea-state and thus, the effects of nonlinear amplifications and wave breaking become ubiquitous. Conversely, in milder sea-states, the prominence of such effects is reduced, leading to smaller deviations in the distributions of crest heights experimentally and numerically.

If we begin by analysing the numerically-generated crest heights shown in Fig. 9(a), it is observed that small crest heights, $\eta_c/H_s < 0.2$, are amplified beyond second-order experimentally as indicated by values of $\Delta > 0$. In fact, amplifications up to $\Delta = 0.1$ are observed, highlighting the importance of higher order nonlinearities in extreme seas.

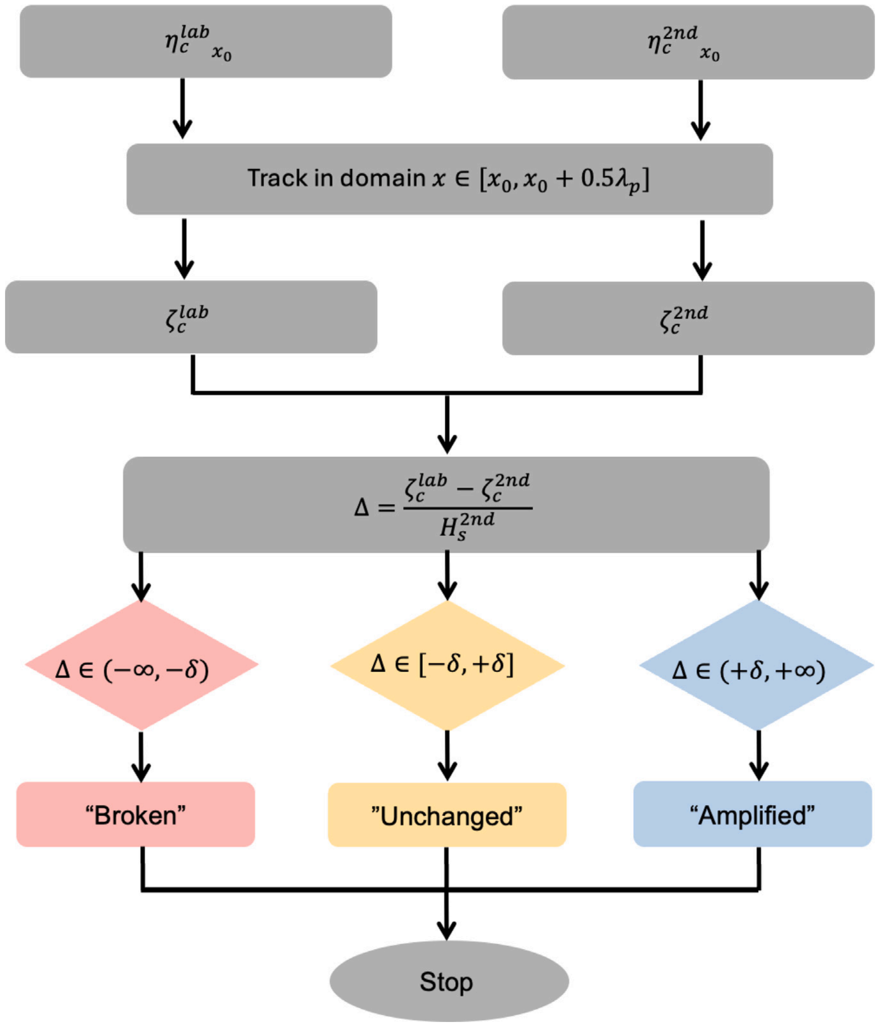

Fig. 8. Schematic summarising the proposed wave classification algorithm.

Conversely, for larger crest heights, $\eta_c/H_s > 0.4$, although nonlinearity is expected to be of importance for these waves, further amplification is not observed due to the limiting effect of wave breaking. This is illustrated by values of $\Delta < 0$. Now examining where the corresponding experimental waves lie in Fig. 9(b), the converse trend is observed. The smallest experimental crest heights are shown to originate from the largest numerical equivalents. These waves are associated with $\Delta < 0$, indicating that the largest numerical crests are not associated with the largest experimental crests since these waves have dissipated significant amounts of energy following wave breaking initiation experimentally. Instead, the largest experimental crests (shown in blue) originate from the smallest numerical crests which have experienced significant nonlinear amplification, denoted by $\Delta > 0$. These findings also support previous work by Holthuijsen and Herbers (1986), who compared the joint probability density function of breaking and non-breaking waves for waves measured in the North Sea.

An aspect to highlight is the trends observed in the left side of Fig. 9(a) for $T_{tt}/T_p < 0.7$. The plot shows a greater occurrence of breaking events in this region, denoted with $\Delta < 0$. Considering that η_c/T_{tt} is a measure of local steepness, this shows the importance of wave breaking in steep waves modelled numerically. Similarly for $T_{tt}/T_p < 0.7$ in Fig. 9(b), experimental waves have been amplified.

Overall, Fig. 9 demonstrates that the effects of wave breaking and amplification result in a notable redistributions of crest heights. This redistribution is associated with discrepancies between experimentally-observed crest heights and second-order prediction as low as $-0.57H_s$ of the second-order prediction.

To further consolidate these findings, the probability density function of each population of waves is illustrated in Fig. 10 for $k_pd = 1.22$, $\sigma_\theta = 10°$, $S_p = 0.04$ for all waves in black, "broken" waves in red and "amplified" waves in blue. Firstly considering the entire population of waves, it is observed that the distribution is positively skewed, consistent with conventional crest height distributions such as Rayleigh (Longuet-Higgins, 1952) and Forristall (Forristall, 2000). However, considering the conditional probability density of "broken" waves compared to "amplified" waves, it is observed that their distribution is more positively skewed, reflected by a heavier tail. In addition, the distribution of "broken" waves is more narrow, with a smaller associated standard deviation. Conversely, the distribution of "amplified" waves exhibits a more symmetric distribution at the tails. In examining the modes of each population, the population of "broken" waves exhibits a smaller value compared to that of "amplified" waves, as a consequence of the energy dissipation process which reduces crest heights. Given that the total population consists of a combination of both categories of waves, it is expected that the associated mode will lie between that of "broken" and "amplified" waves.

These results are consistent for all directional spreads. As discussed by Latheef and Swan (2013) and Karmpadakis et al. (2019), the influence of increased directionality is analogous to a reduction in steepening. As such, it is expected that the occurrence of both wave breaking and wave amplification will be more prevalent in less directional seas, albeit across different values of η_c/H_s. Although directionality is expected to influence the number of waves that experience wave

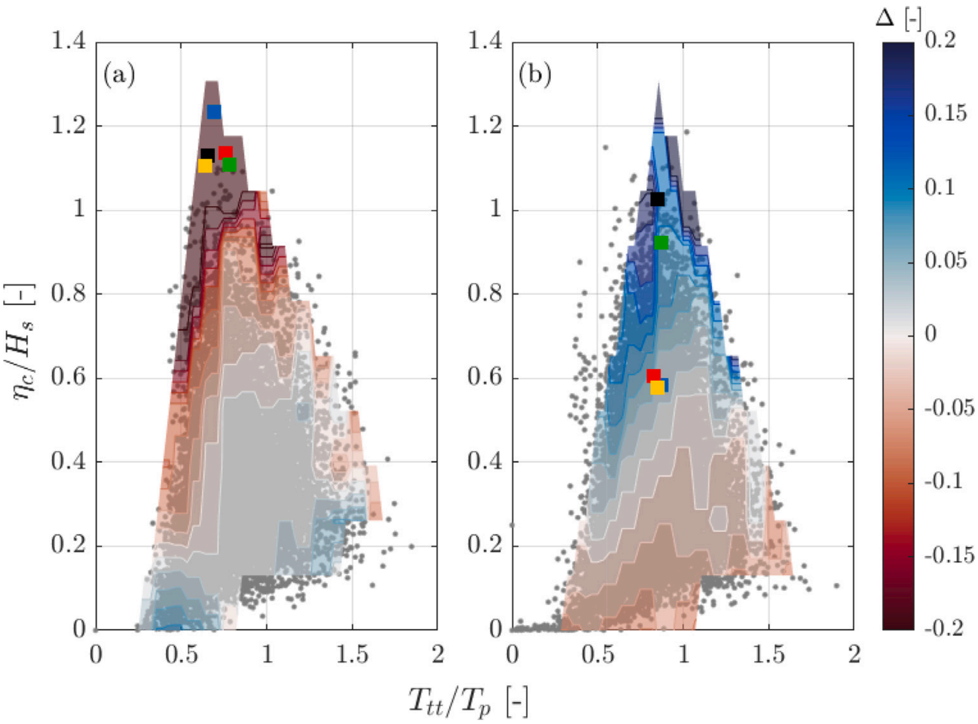

Fig. 9. Scatter plot of normalised crest heights, η_c/H_s, plotted against the normalised trough-to-trough wave period, T_{tt}/T_p, for (a) numerical and (b) experimental data, for σ_θ = 10°, k_pd = 1.22, S_p = 0.05. The contours corresponds to the parameter, Δ. The 5 largest waves numerically are shown in square markers.

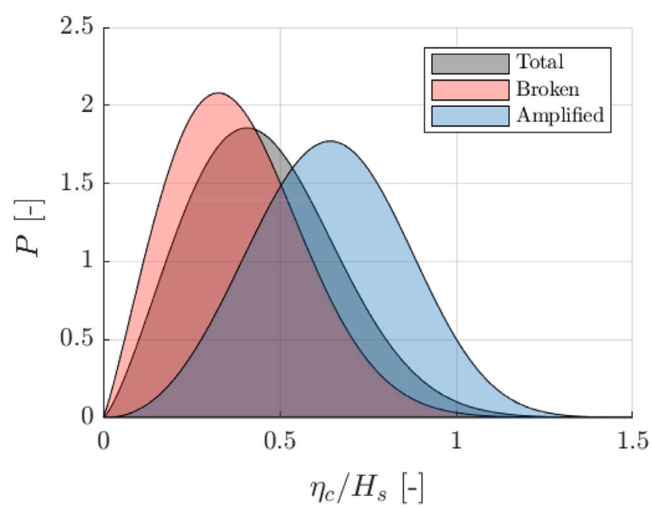

Fig. 10. Probability density function for the normalised crest heights for σ_θ = 10°, k_pd = 1.22, (a) S_p = 0.04. The distribution of all waves, "broken" and "amplified" waves is shown in black, red and blue, respectively.

breaking and amplification, the distribution of these populations with respect to η_c/H_s is shown to be consistent across the directional spread cases investigated.

4.2. Influence of wave breaking on wave–wave interactions

The skewness, λ_3, and (excess) kurtosis, λ_4, of the sea-states can be computed from the time history of the water surface elevation, $\eta(t)$ as defined by:

$$\lambda_3 = \frac{\overline{\eta(t)^3}}{\sigma_\eta^3}, \tag{19}$$

$$\lambda_4 = \frac{\overline{\eta(t)^4}}{\sigma_\eta^4} - 3, \tag{20}$$

where σ_η represents the standard deviation of the surface elevation and the over-bars imply statistical averages.

According to Fedele and Tayfun (2009) in the context of potential theory, the skewness coefficient reflects effects primarily associated with bound nonlinearities. On the other hand, the (excess) kurtosis consists of a dynamic component due to third-order quasi-resonant wave–wave interactions and a bound component from second-order and third-order bound terms (Fedele et al., 2016). Thus, the presence of higher-order effects act to increase the values of skewness and kurtosis beyond the zero value expected in a linear (Gaussian) sea-state. To investigate the prevalence of these effects, Fig. 11 reflects the variation in the skewness and kurtosis with sea-state steepness, $k_1\sigma_\eta$, where k_1 is the wavenumber corresponding to the spectral mean period, T_1.

The coefficient of skewness is observed to linearly increase with increasing sea-state steepness. This is consistent with previous findings of Srokosz and Longuet-Higgins (1986). Based on this data, the measured skewness can be approximated as:

$$\lambda_{3F} = 3.09k_1\sigma_\eta - 0.03. \tag{21}$$

This demonstrates minor deviations from the theoretical result for deep-water narrow-banded sea-states given as $\lambda_{3d} = 3k_1\sigma_\eta$ by Fedele et al. (2016). Conversely, the coefficient of kurtosis is shown to initially increase up to values of $k_1\sigma_\eta \approx 0.07$. Subsequently, a decrease in kurtosis is observed with increasing sea-state steepness. This indicates that higher-order wave–wave interactions act to increase the nonlinearity of the sea-state in the absence of significant wave breaking. However, in much steeper seas where significant wave breaking is prevalent, although skewness is largely unaffected, kurtosis is significantly reduced. This is because wave breaking is a dynamic phenomenon and acts to curtail the large positive surface elevations and hence reduce λ_4. Previous work by Socquet-Juglard et al. (2005) considered kurtosis to be proportional to $(k_1\sigma_\eta)^2$; however, the results of this work indicate that in the context of the steepest sea-states where wave breaking

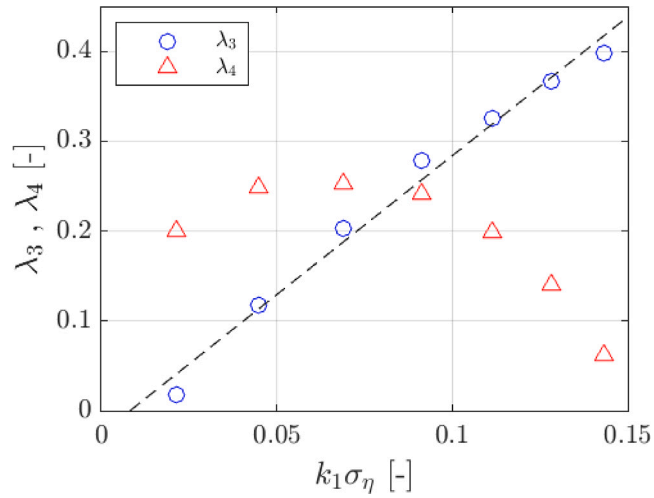

Fig. 11. Variation of skewness, λ_3, and kurtosis, λ_4, shown in blue and red, respectively, with $k_1\sigma_\eta$ for sea-states with $\sigma_\theta = 10°$, $k_pd = 1.53$. The linear fit for λ_3 given by Eq. (21) is shown in a black dashed line.

effects dominate, the evolution of kurtosis is inversely proportional to $k_1\sigma_\eta$.

4.3. Probability and associated energy dissipation of "broken" waves

Thus far, the prevalence of wave breaking and its influence on the distribution, rank and wave–wave interactions is established. However, a fundamental aspect to ascertain is the breaking probability and their associated extent of energy dissipation for a given sea-state. Previous work by Schwendeman and Thomson (2017) has outlined the strong correlation of wave breaking prevalence with the significant wave steepness for a broad range of wave conditions in the field.

The probability of breaking, P_{br}, and amplification, P_{amp} for a given sea-state is calculated as the ratio of the total number of "broken" and "amplified" waves, respectively, classified according to the algorithm in Fig. 8, to the total number of waves. The variation in the probability of breaking, P_{br}, and amplification, P_{amp}, with sea-state steepness is shown in Fig. 12(a) and (b), respectively. Error bars are included, which correspond to the magnitude of P_{br} and P_{amp} for $S_p = 0.01$. This represents the potential misclassification of small waves in mild sea-states. The probability of wave breaking increases with increased sea-state steepness such that probabilities as large as 22% are observed in extreme seas. The values presented in this work are marginally higher than those outlined by Banner et al. (2000) for wind-generated waves in the field. This is to be expected given that the waves considered in this work are in finite water depths. This hypothesis is further consolidated by Filipot et al. (2010) who considered waves in the field for a broad range of water depth regimes. Similarly, the probability of amplification, as shown in Fig. 12(b), increases with increased sea-state steepness such that probabilities as large as 24% are observed in extreme seas.

To quantify the extent of energy dissipation, we examine the total normalised energy of the sea-state defined as:

$$E_X = \sum (\zeta_c/H_s)^2/N, \tag{22}$$

where E_X is the energy and the subscript X indicates "broken" or "amplified", E_{br} and E_{amp}, respectively.

The summation in Eq. (22) is conducted across sub-population X of waves and N is the total number of waves in the full population. The variation in the total normalised energy, E_X, with sea-state steepness, S_p is shown in Fig. 12(c) and (d) for the population of "broken" and "amplified" waves, respectively. Experimental and numerical results are shown in blue and red lines, respectively. Numerically, analysing the variation of E with increased sea-state steepness provides the contribution of second-order bound nonlinearities. However, experimentally, this variation further highlights the increased prevalence of higher-order contributions and wave breaking with increased steepness, which are effects not included numerically.

To quantify the extent of breaking energy dissipation, we consider the energy evolution of "broken" waves, E_{br} with sea-state shown in Fig. 12(c). Firstly examining the trend in E_{br} numerically, we observe an increase with increasing S_p as a consequence of the presence of second-order bound nonlinear terms. If we now examine this experimentally, although the same general trend is observed, numerical values of E_{br} are always greater than those experimentally. In other words, experimentally, the increase in crest heights with increasing sea-state steepness is less than predicted by theory, as a consequence of the limiting effects of wave breaking. As such the variation in the value of E_{br} numerically and experimentally can be used as a proxy to quantify the extent of wave breaking energy dissipation, as indicated by the grey shaded area on Fig. 12(c). We observe that the extent of wave breaking energy dissipation is comparable in up to moderate sea-states ($S_p \leq 0.03$), however, significant increases in energy dissipation are observed in steeper sea-states ($S_p > 0.03$). The extent of this is more pronounced as the sea-state steepness is increased further, with a maximum discrepancy in the value of E_{br} between the two datasets observed at $S_p = 0.06$ such that the energy content experimentally is 51% of that predicted numerically.

To consider the influence of higher-order contributions to the sea-state energy content, we examine the energy evolution of "amplified" waves, E_{amp} with steepness, S_p, shown in Fig. 12(d). Similar to "broken" waves, the energy content of the sea-state increases with increased sea-state steepness, both experimentally and numerically. However, the key distinction in the context of "amplified" waves is that for all sea-states, experimental values of E_{amp} exceed those calculated numerically. Hence, in a similar manner to the consideration of breaking energy dissipation, the variation in the value of E_{amp} numerically and experimentally can be used as a proxy to quantify the additional energy due to wave amplification experimentally, as indicated in the grey shaded area on Fig. 12(d). These results indicate that although the importance of higher-order effects are minor in mild sea-states, $S_p \leq 0.02$, their significance increases with increasing sea-state steepness. In fact, in the steepest sea-states, $S_p = 0.06$, the total normalised energy content experimentally can be greater than double that predicted by second-order numerical simulations.

The energy dissipation calculated in the present model may be compared to the commonly adopted phase-averaged model, SWAN (Booij et al., 1999). The dissipation of energy due to whitecapping is accounted for by the spectral dissipation term, S_{ds}, defined according to the formulation of Komen et al. (1984) as:

$$S_{ds}(\omega,\theta) = -C_{ds}\overline{\omega}\left(\frac{\omega}{\overline{\omega}}\right)^2\left(\frac{\hat{\alpha}}{\alpha_{\hat{P}M}}\right)^2 S_{\eta\eta}(\omega,\theta), \tag{23}$$

where C_{ds} is the coefficient for whitecapping dissipation, $\overline{\omega}$ is the mean angular frequency, $\hat{\alpha} = E\overline{\omega}^4 g^{-2}$ is a measure of wave steepness, $E = \int_0^{2\pi}\int_0^{\infty} S_{\eta\eta}(\omega,\theta)d\omega d\theta$ is the energy of the spectrum, g is the gravitational acceleration and $\hat{\alpha}_{PM}$ is the corresponding steepness of the Pierson and Moskowitz (1964) spectrum. The values of C_{ds} and $\hat{\alpha}_{PM}$ are 2.36×10^{-5} and 3.02×10^{-3}, respectively, as implemented in SWAN. Utilising this formulation, the spectral dissipation term is normalised and integrated across the frequency range such that the total proportional energy dissipated by a sea-state is:

$$\delta^*_{br} = \int_0^{2\pi}\int_0^{\infty} \omega^{-1} S_{ds}(\omega,\theta)d\omega d\theta. \tag{24}$$

The value of δ^*_{br} depends critically on the high-frequency cut-off used (Young and Banner, 1992). To ensure consistency with SWAN, this limit is set to 1 Hz in field scale.

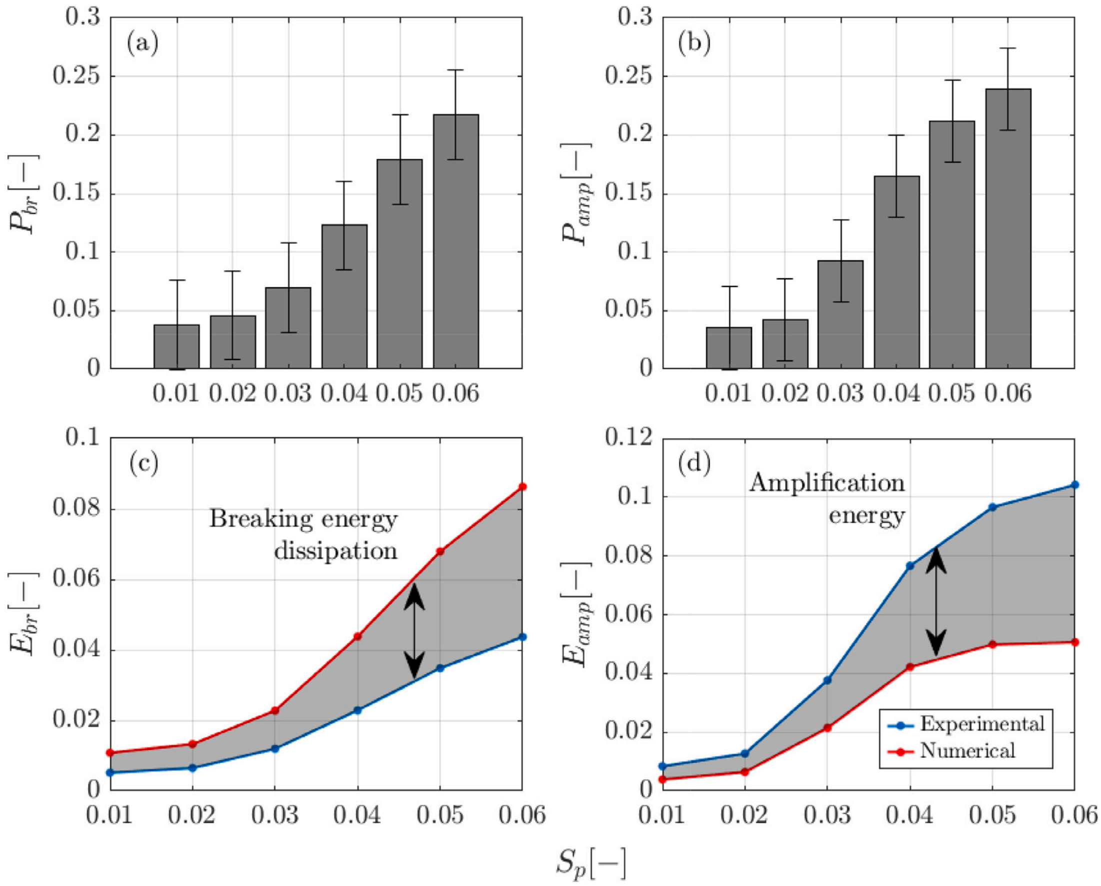

Fig. 12. Variation in the probability of (a) breaking, P_{br} and (b) amplification, P_{amp}, with sea-state steepness. Error bars correspond to magnitude of P_{br} and P_{amp} for $S_p = 0.01$, respectively. Variation in the total normalised energy of (c) "broken", E_{br} and (d) "amplified", E_{amp} waves with sea-state steepness. Experimental and numerical results are shown in blue and red lines, respectively. Extent of breaking energy dissipation and energy associated with wave amplification is shown in the grey shaded area in (c) and (d), respectively. Results correspond to sea-states with $\sigma_\theta = 10°$, $k_p d = 1.22$.

In the present model, the total proportional energy dissipated by a sea-state is determined by extending Eq. (22) such that:

$$\delta_{br} = \frac{\sum\left(\frac{\zeta_c^{lab}}{H_s^{lab}} - \frac{\zeta_c^{2nd}}{H_s^{2nd}}\right)^2_{br}}{\sum\left(\frac{\zeta_c^{2nd}}{H_s^{2nd}}\right)^2_{tot}}, \quad (25)$$

where the subscript "*br*" indicates values associated with breaking waves only and "*tot*" indicates values associated with all waves in the sea-states. In essence, Eq. (25) provides a measure of the energy lost through breaking normalised by the total energy of the sea-state. Fig. 13 compares the evolution of δ_{br} and δ^*_{br} with increasing sea-state steepness, S_p. The value of δ_{br} is adjusted to account for the misclassification of waves in very mild sea-states, as discussed earlier.

Similar trends in the evolution of δ_{br} and δ^*_{br} are observed such that an exponential growth is seen with increasing S_p. The correspondence of our results to the SWAN model is promising, given that it is a well-established model extensively validated against a broad range of experimental and field data (Booij et al., 1999). This is particularly encouraging considering that no calibration of the default parameters was performed, despite their inherent sensitivity to sea-state conditions. Some discrepancies are observed, particularly in steep sea-states. This may be explained by the presence of overturning waves in the present dataset which experience greater energy dissipation compared to spilling breakers (Duncan, 1981). Conversely, the dissipation term in the SWAN model is for whitecapping only, generally associated with spilling breakers. Overall, the results of this investigation demonstrate the applicability of the present formulation to describe breaking energy dissipation, which may then be integrated into numerical wave models in future works.

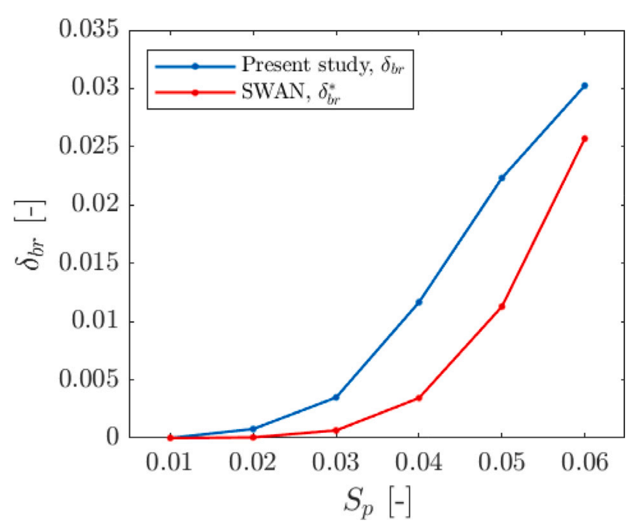

Fig. 13. Variation in the total proportional energy dissipation with sea-state steepness, S_p, for $\sigma_\theta = 10°$, $k_p d = 1.22$. Results corresponding to the present model, δ_{br}, and the SWAN model, δ^*_{br}, are shown in blue and red, respectively.

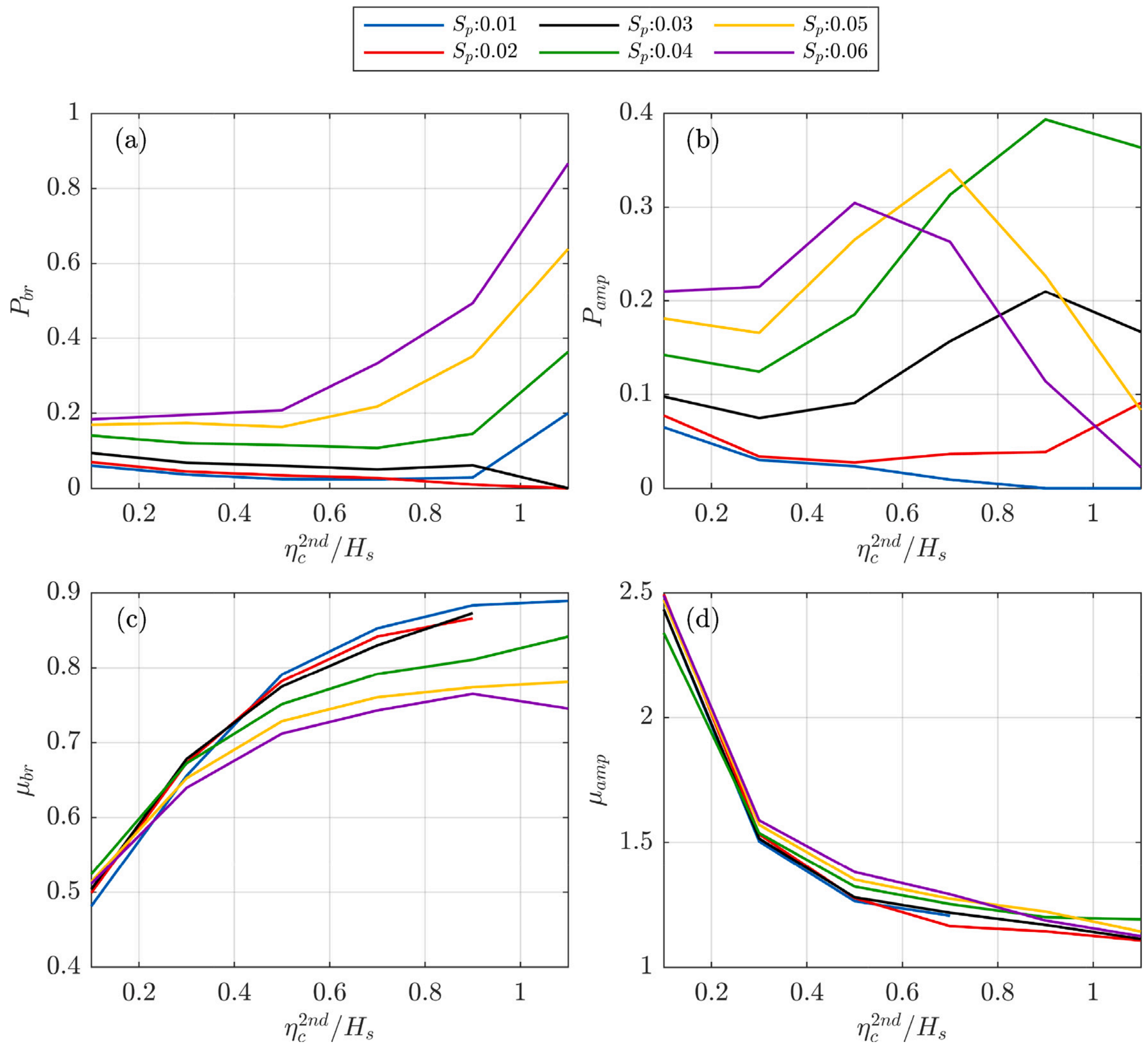

Fig. 14. Probability of (a) "broken" and (b) "amplified" waves and the mean value of the ratio, r, for (c) "broken" and (d) "amplified" waves conditional on their normalised second-order crest height, $\eta_c^{2\mathrm{nd}}/H_s$, for $\sigma_\theta = 10°$, $k_p d = 1.22$.

In order to more formally investigate the probabilities of wave breaking and nonlinear amplification, the domain of normalised second-order crest heights at the central gauge, $\eta^{2\mathrm{nd}}/H_s$, is partitioned into intervals of width $\Delta\eta^{2\mathrm{nd}}/H_s = 0.2$. In doing so, the wave classification algorithm described in Section 3 can be implemented within each interval. Subsequently, the probability of wave breaking and amplification within an interval is defined as the ratio of the number of "broken" and "amplified" waves, respectively, to the total number of waves in the interval. These results are illustrated in Fig. 14(a) and (b) for "broken" and "amplified", respectively, corresponding to $\sigma_\theta = 10°$, $k_p d = 1.22$ for increasing sea-state steepness as shown by the line colour.

The probability of breaking, P_{br}, demonstrates that in mild seas, $S_p \le 0.03$, the presence of wave breaking is minimal, even for relatively large values of $\eta_c^{2\mathrm{nd}}/H_s$. Conversely, for moderate to extreme seas, $S_p > 0.03$, the probability of wave breaking is notable and is shown to increase with normalised second-order crest magnitude $\eta_c^{2\mathrm{nd}}/H_s$ and with increasing sea-state steepness.

In considering the probability of wave amplification, P_{amp}, for the smaller (second-order) waves, there is a clear increase in the probability of wave amplification for increasing sea-state steepness. However, the relative magnitude of the probability of amplification for the largest second-order waves that lie in the tail of the distribution is greater with increased steepness, provided $S_p \le 0.04$. This indicates that the relative importance of higher order nonlinearities is greater in steeper seas. However, in considering the steeper sea-states, $S_p > 0.04$, although these seas present a higher occurrence of wave amplification for the smallest (second-order) waves compared to less steep seas, these probabilities significantly reduce with increasing $\eta_c^{2\mathrm{nd}}/H_s$. In fact, in the tail of the crest height distribution, the probability of wave amplification is lower with increased sea-state steepness, provided $S_p > 0.04$. Combining these findings with those shown in Fig. 14(a), it is evident that in highly nonlinear seas, waves occurring in the tail of the distribution are not further amplified as their growth is limited by the increased prevalence of wave breaking. This is of importance in selecting individual wave events for design applications in extreme value statistics. These findings demonstrate that the largest second-order crest heights are not necessarily found in the tail of the experimental crest height distribution.

In addition to investigating the probabilities of these sub-populations, the ratio of experimental to numerical crest heights, r, is of interest. Formally, this is defined as the ratio of the spatial maximum experimental height normalised by the significant wave height of the sea-state, divided by the corresponding normalised crest height numerically as defined by Eq. (26):

$$r = \frac{\zeta_c^{lab}/H_s^{lab}}{\zeta_c^{2\mathrm{nd}}/H_s^{2\mathrm{nd}}}. \tag{26}$$

It is important to note that the parameter r is different from r_{KS20}, which considered the ratio at a local spatial location, as opposed to the global maximum crest height. The mean value of r in each interval for "broken", μ_{br}, and "amplified", μ_{amp}, waves is illustrated in Fig. 14(c) and (d), respectively. In general, across the range of normalised second-order crest height distribution, the magnitude of μ_{br} is lower with increased sea-state steepness. This indicates that in steeper seas, not only is the likelihood of wave breaking greater, but also the reduction in the crest height relative to second-order is greater as a consequence of wave breaking, indicating a stronger influence of the breaking effect and an increased discrepancy from second-order theory. In analysing the variation of μ_{br} with η_c^{2nd}/H_s, it is clear that smaller (second-order) waves are associated with lower μ_{br} values. However, this does not necessarily mean these waves are dissipating more energy. Rather, it is more relative to the magnitude of the (second-order) crest height, ζ_c^{2nd}, since the value of r is normalised by this value. In the case of "amplified" waves, the extent of the influence of higher order nonlinearities is marginally greater for increased steepness, S_p. Relative to η_c^{2nd}/H_s, the reduction in μ_{amp} with increasing (second-order) crest height indicates a reduction in the increase of the experimental crest height relative to the magnitude of ζ_c^{2nd}. However, a plateau towards $\mu_{amp} = 1.1$ is observed in the tail of the distribution.

5. Breaking wave modelling

The wave classification algorithm proposed can be used to model breaking waves. The concept behind the model development is to formulate a transformation consisting of a statistical distribution that may be applied to existing second-order models that transforms the predicted crest heights from these models into crest heights that closely align with that of real waves. The proposed formulation in this study follows a mixture model structure to model the full range of crest heights. This transformation seeks to capture both the effects of higher-order nonlinearity and wave breaking characteristic of real sea-states, that are not adequately captured in existing second-order crest height models, in a novel and innovative way.

5.1. Model development

The model development has been conducted as follows:

1. An aligned dataset is generated such that each numerically-simulated second-order crest is aligned to its corresponding laboratory-generated crest as outlined in Section 3.
2. The total population of the normalised second-order simulated crest heights, ${\eta_c}^{2nd}/H_s$, is partitioned into intervals of width $\Delta{\eta_c}^{2nd}/H_s = 0.2$.
3. Within each interval, the parameter Δ defined by Eq. (18) is calculated for each pair of second-order and corresponding experimentally-generated crest heights.
4. The value of Δ is utilised to define three populations of waves: "broken", "unchanged" or "amplified".
5. The probability of breaking, P_{br}, and amplification, P_{amp}, within each interval is determined based on the ratio of the number of "broken" and "amplified" waves, respectively, to the total number of waves in the interval.
6. The value of the ratio r defined by Eq. (26) is calculated to determine the relative scaling of experimental to numerical crest heights.
7. The distribution of r within each interval for each population of waves is plotted and a reasonable statistical distribution is fitted to this ratio.

Steps 1–6 have been extensively discussed in Sections 3 and 4. Hence, this section will focus on addressing the final step inference. Implementing the wave classification algorithm as denoted by steps 1–6, we can model the distribution of "broken" and "amplified" waves within each η_c^{2nd}/H_s interval. These are illustrated in Fig. 15 for $\sigma_\theta =$ 10°, $k_p d = 1.22$, $S_p = 0.04$. Each subplot corresponds to an η_c^{2nd}/H_s interval, with the histogram of "broken" and "amplified" wave populations shown in red and blue, respectively. It is observed that the distribution of "broken" waves is negatively skewed whereas "amplified" waves are positively skewed. Upon investigation, it is found that a beta and gamma distribution are appropriate to model the distribution of "broken" and "amplified" waves within each interval, respectively. These fitted distribution are shown using a solid line in Fig. 15 in red ("broken") and blue ("amplified"). These results reflect good agreement to the actual population distributions. As such, these findings are utilised as the foundation for model development.

The distribution of the sub-population of "broken"and "amplified" waves are fitted to beta ($\tilde{B}(\alpha, \beta)$) and gamma ($\tilde{\Gamma}(\nu, \psi)$) distributions, respectively. Thus, the following mixture model is proposed:

$$f = \sum_{i=1}^{I} \Pi_i \cdot \left(P_{br,i} \cdot \tilde{B}\left(\alpha_i, \beta_i\right) + P_{amp,i} \cdot \tilde{\Gamma}\left(\nu_i, \psi_i\right) + P_{n,i} \cdot 1 \right), \tag{27}$$

where Π_i is a rectangular function with value 1 in interval i and 0 otherwise. The total number of intervals is denoted by I. Additionally, $\tilde{B}\left(\alpha_i, \beta_i\right)$ and $\tilde{\Gamma}\left(\nu_i, \psi_i\right)$ denote the beta and gamma distributions for interval i, respectively. The full model parameters as obtained from the experiments are provided in Appendix B. Similarly, $P_{X,i}$, is the probability of X in interval i defined as:

$$\text{For } X = \begin{cases} \text{“broken” }, & P_{br,i} \\ \text{“amplified”}, & P_{amp,i} \\ \text{unchanged }, & P_{n,i}. \end{cases}$$

These probabilities must satisfy the condition:

$$\forall i \in I; P_{br,i} + P_{amp,i} + P_{n,i} = 1. \tag{28}$$

5.2. Model application and validation

Following the inference of the distribution parameters, the model can then readily be applied as follows:

1. The initial crest height distribution is obtained from SORWT simulations, or more practically by applying a second-order crest height model such as Forristall (2000), based on the characteristics of the sea-state of interest.
2. The total population of the normalised crest heights, η_c^{2nd}/H_s, is partitioned into intervals of width $\Delta\eta_c^{2nd}/H_s = 0.2$.
3. Within each interval, second-order crest heights are randomly split into "broken", "unchanged" or "amplified" sub-populations so the number of waves in each interval correspond to the probabilities P_{br}, P_n and P_{amp} in each interval obtained in the model development phase, as indicated in Fig. 14(a) and (b).
4. Within each bin, every wave is multiplied by r, given by the $\tilde{B}\left(\alpha_i, \beta_i\right)$ and $\tilde{\Gamma}\left(\nu_i, \psi_i\right)$ distributions for "broken" and "amplified" waves, respectively.
5. Once all transformations for "breaking" and "amplified" waves are applied for each interval, crest heights are re-ordered and the new crest height distribution is plotted.
6. This methodology is repeated with 100 runs for each sea-state. This ensures that issues of statistical random sampling associated with randomly selecting "broken" and "amplified" waves in each interval (step 3) is overcome.

The selection of 100 repetitions of the aforementioned methodology is shown to converge the results of the normalised crest height distribution with a mean error of below 10^{-5} across all waves and a maximum discrepancy of $O(10^{-3})$ in the tail of the distribution, even for extreme sea-states where significant nonlinear modifications to the waves occur through the modelling procedure. Hence, the choice of 100 repetitions

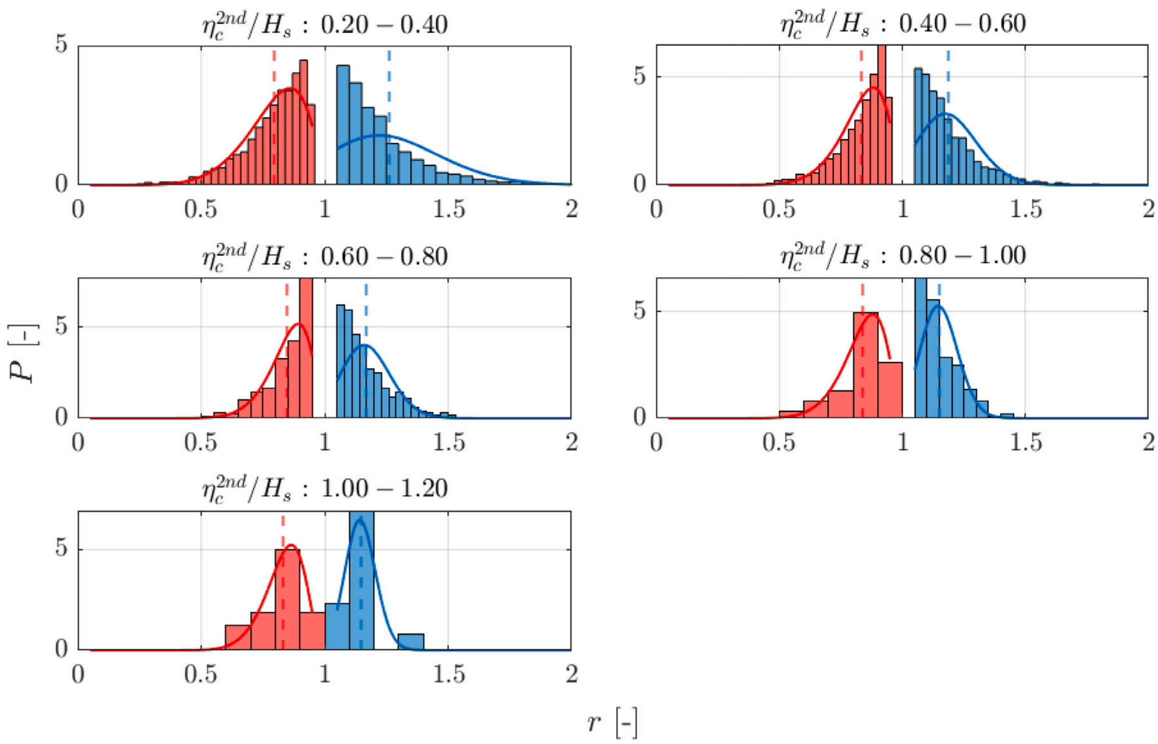

Fig. 15. Histogram of the distribution of the ratio of laboratory to second-order simulated crest heights, r, for $\sigma_\theta = 10°$, $k_p d = 1.22$, $S_p = 0.04$, with each subplot corresponding to an interval value of the normalised numerical crest height. The distribution of "broken" and "amplified" waves, along with the fitted β and γ distributions, is shown in red and blue, respectively. The mean value of r for each sub-population is shown in a dashed line where values corresponding to "broken", μ_{br}, and "amplified", μ_{amp}, are shown in red and blue, respectively.

is deemed sufficient to ensure the statistical reliability of the model implementation.

To validate the accuracy of this model, the transform function is applied to SORWT simulations for a range of sea-states of varying directionality, effective water depth and steepness. Fig. 16 compares the experimental crest height distribution (shown in black markers) to the commonly adopted Rayleigh (Longuet-Higgins, 1952) and Forristall (Forristall, 2000) crest height distributions. The results according to SORWT are shown in green, with the proposed mixture model shown in purple.

In sea-states of small to moderate steepnesses, such as those illustrated in Fig. 16(a) and (b), the importance of nonlinear effects beyond second-order becomes evident as shown by an underestimation in the second-order Forristall distribution and SORWT. However, the proposed model is shown to overcome most of this discrepancy by providing a much closer distribution relative to experimental observations. The success of the model continues to hold for highly nonlinear seas, as shown in Fig. 16(c), and extreme seas dominated by breaking effects as shown in Fig. 16(d). The mixture model is shown to capture the full distribution of crest heights in these cases for up to small probabilities of exceedance, $Q = 10^{-4}$, where the use of SORWT is unable to capture the observed higher order nonlinearities and breaking effects. The accuracy of these results is similar to that of Karmpadakis and Swan (2022), which is based on an extensive dataset consisting of both experimental and field measurements. However, the waves generated do not employ the phase alignment method which is critical for the implementation of the methodology of the present work. Thus, the coupling between laboratory and numerical data in the present method carries the additional information of having identified the nature of waves ("broken" and "amplified").

The applicability of the mixture model can be further quantified by considering Fig. 17, demonstrating the variation of the crest height corresponding to $Q = 10^{-3}$ with sea-state steepness, S_p, for $\sigma_\theta = 10°$, $k_p d = 1.22$. Results corresponding to the experimental data, the mixture model and the Forristall distribution are shown in black, green and red, respectively. It is well known that the commonly adopted Forristall model significantly underestimates crest heights, as is evident here when comparing its predictions to experimental data. The extent of these underestimations increase with sea-state steepness up to the domination of wave breaking effects, which is $S_p = 0.04$ in this case. This underestimation is then partially counteracted by wave breaking effects in sea-states of higher steepness. However, in examining the performance of the mixture model, it is shown to provide significant improvements to second-order predictions across a wide range of sea-state steepnesses, $S_p \leq 0.05$. However, in the most extreme seas, $S_p = 0.06$, the Forristall distribution performs marginally better. This is coincidental since the effects of wave breaking act to outweigh some of the higher-order effects that the Forristall distribution neglects (Karmpadakis, 2019). Comparatively, the mixture model in extreme seas experiences a small positive bias. This can be explained by the practical limit of 20,000 waves per sea-state in this study. Additional data for extreme cases will further improve the level of agreement by considering wave extremes. However, despite the limitations in the model in such cases, the classification methodology proposed can provide significant insight into the physical characteristics of "broken" waves as demonstrated in Section 4. Importantly, the method opens up new horizons for further data integration and model development. Moreover, the broad agreement of the results of the mixture model to the experimental data shown in Fig. 16, and the consistency between the breaking probabilities and energy dissipation presented in Section 4 to literature, highlight the generalisability of the proposed methodology to future works. For the specific application of this method in the present work, we cover a broad range of effective water depths, $k_p d \in [1.02, 1.53]$, sea-state steepnesses, $S_p \in [0.01, 0.07]$, and directional spreading, $\sigma_\theta \in [10, 20]$. Thus, the findings of this work encompass an extensive range of cases which are representative of real sea-state conditions.

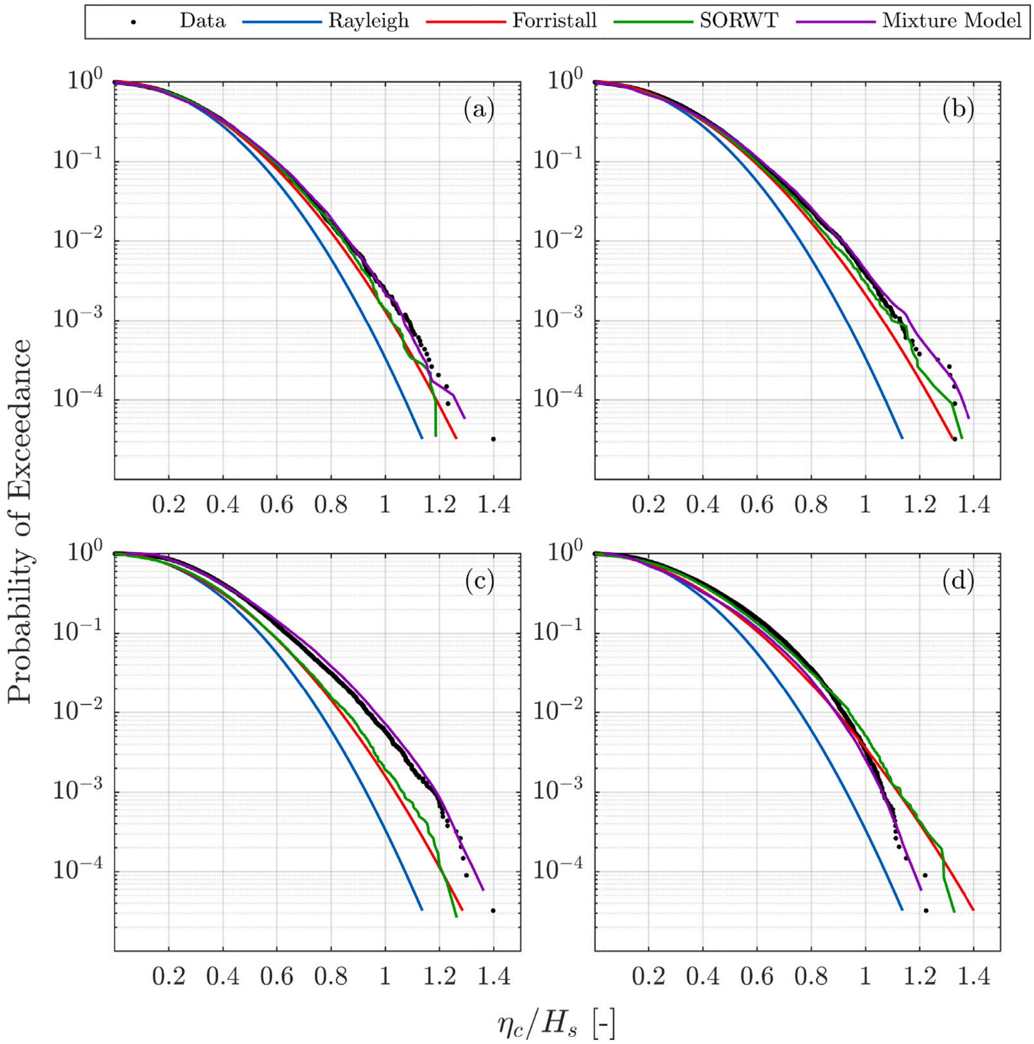

Fig. 16. Crest height distribution for (a) $\sigma_\theta = 10°$, $k_pd = 1.02$, $S_p = 0.02$, (b) $\sigma_\theta = 20°$, $k_pd = 1.02$, $S_p = 0.03$, (c) $\sigma_\theta = 10°$, $k_pd = 1.53$, $S_p = 0.04$, and (d) $\sigma_\theta = 10°$, $k_pd = 1.22$, $S_p = 0.06$. Experimental data is shown in black markers. The blue, red and green lines correspond to the crest height distribution of Rayleigh (Longuet-Higgins, 1952) Forristall (Forristall, 2000) and SORWT, respectively. The crest height distribution according to the mixture model is shown in purple.

6. Conclusion

This study presents a novel methodology to identify and classify breaking wave events in short-crested seas in intermediate water depths, through the combination of laboratory experiments and second-order numerical simulations. By enabling a direct wave-by-wave comparison, the proposed approach allows for robust classification of individual waves and the quantification of both breaking probability and associated energy dissipation across a wide range of sea-state conditions.

The analysis reveals that wave breaking becomes increasingly prevalent and energetically significant with rising sea-state steepness. In the steepest sea-states considered, breaking probabilities exceeded 20%, highlighting the dominant role of dissipation under extreme conditions. Moreover, a consistent spatial downshift in the location of maximum experimental crest heights relative to second-order predictions is observed, underscoring the limitations of conventional single-point analyses and emphasising the importance of spatially-resolved wave tracking.

Building on these insights, a new statistical mixture model is developed. This model incorporates the distinct behaviours of broken and amplified waves to transform second-order numerical predictions into realistic crest height distributions. The proposed model has been shown to provide considerable improvements over established models, particularly in capturing the tail behaviour under extreme conditions. Even in the steepest sea-states, the model remains reliable, while providing a physical interpretation of crest height statistics that accounts for both breaking energy dissipation and nonlinear amplification.

Overall, this work offers a comprehensive framework for the characterisation of wave breaking and its statistical representation. The methodology is directly applicable to the design and safety assessment of coastal and offshore infrastructure, where the occurrence of breaking can significantly alter loading conditions. Importantly, the findings establish a foundation for future integration with field measurements and the development of probabilistic tools in coastal engineering design.

CRediT authorship contribution statement

Umniya Al Khalili: Writing – original draft, Visualization, Investigation, Formal analysis, Conceptualization. **Ioannis Karmpadakis:** Writing – review & editing, Supervision, Methodology, Data curation, Conceptualization.

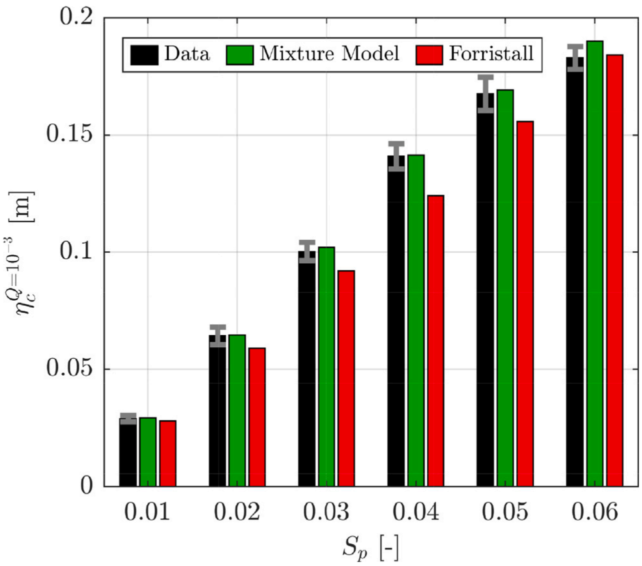

Fig. 17. Variation of the crest height corresponding to $Q = 10^{-3}$ with sea-state steepness, S_p, for $\sigma_\theta = 10°$, $k_pd = 1.22$. Results corresponding to the experimental data, the mixture model and the Forristall distribution (Forristall, 2000) are shown in black, green and red, respectively. Error bars corresponding to the 95% confidence interval for the data are added in grey.

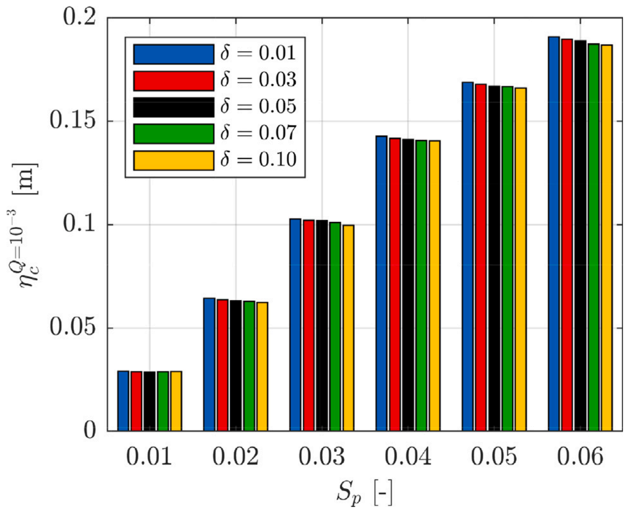

Fig. 18. Variation of crest height corresponding to $Q = 10^{-3}$ with sea-state steepness, S_p, for $\sigma_\theta = 10°$, $k_pd = 1.22$. Each colour corresponds to a variable buffer size, δ.

Declaration of competing interest

The authors declare that they have no known competing financial interests or personal relationships that could have appeared to influence the work reported in this paper.

Acknowledgments

The authors thank A.Babanin and D.Liberzon for useful discussions and recommendations.

Appendix A. Buffer region for wave modelling

In order to determine the influence of the buffer region, δ. on the applicability of the model, the transform function given by Eq. (27) is imposed on SORWT simulations using variable δ values. The results of this analysis are shown in Fig. 18 which demonstrates the variation in the calculated crest height associated with a probability of exceedance of $Q = 10^{-3}$, with the sea-state steepness. Each colour corresponds to a variable buffer size, δ.

The findings suggest that the results are overall relatively insensitive to the choice of δ, consistent with previous work by Karmpadakis and Swan (2020). Nevertheless, this study reveals a marginal reduction in crest height with increasing buffer width, implying that the upper limit defining the population of amplified waves is primarily affected. The greater buffer width results in fewer amplified waves being transformed by the model. Despite this, the modelling process remains applicable across different choices of δ, confirming the robustness of the adopted methodology. In this work, a value of $\delta = 0.1$ is used throughout.

Appendix B. Fitted distribution parameters used in wave modelling

The fitted distribution parameters for the proposed new statistical mixture model, along with functions to implement the model, are available as an addendum to the paper at https://github.com/ikarmpadakis/shortcrested_breaking.git.

Data availability

Data will be made available on request.

References

Adcock, T.A., Gibbs, R.H., Taylor, P.H., 2012. The nonlinear evolution and approximate scaling of directionally spread wave groups on deep water. Proc. R. Soc. A: Math. Phys. Eng. Sci. 468 (2145), 2704–2721. http://dx.doi.org/10.1098/rspa.2012.0029.

Airy, G., 1845. Tides and Waves: Extracted from the Encyclopaedia Metropolitana. Vol. 5, B. Fellowes.

Alsina, J.M., Baldock, T.E., 2007. Improved representation of breaking wave energy dissipation in parametric wave transformation models. Coast. Eng. 54 (10), 765–769. http://dx.doi.org/10.1016/j.coastaleng.2007.05.005.

Altomare, C., Scandura, P., Caceres, I., Viccione, G., et al., 2023. Large-scale wave breaking over a barred beach: SPH numerical simulation and comparison with experiments. Coast. Eng. 185, 104362. http://dx.doi.org/10.1016/j.coastaleng.2023.104362.

Andreas, E.L., Edson, J.B., Monahan, E.C., Rouault, M.P., Smith, S.D., 1995. The spray contribution to net evaporation from the sea: A review of recent progress. Bound.-Layer Meteorol. 72, 3–52. http://dx.doi.org/10.1007/BF00712389.

Babanin, A.V., 2011. Breaking and Dissipation of Ocean Surface Waves. http://dx.doi.org/10.1017/CBO9780511736162.

Babanin, A.V., Young, I.R., Banner, M.L., 2001. Breaking probabilities for dominant surface waves on water of finite constant depth. J. Geophys. Res. 106, 11659. http://dx.doi.org/10.1029/2000JC000215.

Baldock, T.E., Holmes, P., Bunker, S., Van Weert, P., 1998. Cross-shore hydrodynamics within an unsaturated surf zone. Coast. Eng. 34, 173–196. http://dx.doi.org/10.1016/S0378-3839(98)00017-9.

Banner, M.L., Babanin, A.V., Young, I.R., 2000. Breaking probability for dominant waves on the sea surface. J. Phys. Oceanogr. 30, 3145–3160. http://dx.doi.org/10.1175/1520-0485(2000)030<3145:BPFDWO>2.0.CO;2.

Banner, M.L., Gemmrich, J.R., Farmer, D.M., 2002. Multiscale measurements of ocean wave breaking probability. J. Phys. Oceanogr. 32 (12), 3364–3375. http://dx.doi.org/10.1175/1520-0485(2002)032<3364:MMOOWB>2.0.CO;2.

Banner, M.L., Tian, X., 1998. On the determination of the onset of breaking for modulating surface gravity water waves. J. Fluid Mech. 367, 107–137. http://dx.doi.org/10.1017/S0022112098001517.

Barratt, D., Bingham, H.B., Taylor, P.H., Bremer, T.S.V.D., Adcock, T., 2021. Rapid spectral evolution of steep surface wave groups with directional spreading. J. Fluid Mech. 907, A30. http://dx.doi.org/10.1017/jfm.2020.835.

Barthelemy, X., Banner, M., Peirson, W., Fedele, F., Allis, M., Dias, F., 2018. On a unified breaking onset threshold for gravity waves in deep and intermediate depth water. J. Fluid Mech. 841, 463–488. http://dx.doi.org/10.1017/jfm.2018.93.

Battjes, J.A., Groenendijk, H.W., 2000. Wave height distributions on shallow foreshores. Coast. Eng. 40 (3), 161–182. http://dx.doi.org/10.1016/S0378-3839(00)00007-7.

Battjes, J.A., Janssen, J., 1978. Energy loss and set-up due to breaking of random waves. In: Coastal Engineering 1978. pp. 569–587. http://dx.doi.org/10.1061/9780872621909.034.

Battjes, J.A., Stive, M.J.F., 1985. Calibration and verification of a dissipation model for random breaking waves. J. Geophys. Res.: Ocean. (C5), 9159–9167. http://dx.doi.org/10.1029/JC090iC05p09159.

Beach, R.A., Sternberg, R.W., 1996. Suspended-sediment transport in the surf zone: response to breaking waves. Cont. Shelf Res. 16 (15), 1989–2003. http://dx.doi.org/10.1016/0278-4343(96)00029-5.

Benoit, M., Zhang, J., Ma, Y., 2024. Kinematics of nonlinear waves over variable bathymetry. Part I: Numerical modelling, verification and validation. Coast. Eng. 193, 104577. http://dx.doi.org/10.1016/j.coastaleng.2024.104577.

Bihs, H., Kamath, A., Chella, M.A., Aggarwal, A., Arntsen, Ø.A., 2016. A new level set numerical wave tank with improved density interpolation for complex wave hydrodynamics. Comput. & Fluids 140, 191–208. http://dx.doi.org/10.1016/j.compfluid.2016.09.012.

Booij, N., Ris, R.C., Holthuijsen, L.H., 1999. A third-generation wave model for coastal regions: 1. model description and validation. J. Geophys. Res.: Ocean. 104 (C4), 7649–7666. http://dx.doi.org/10.1029/98JC02622.

Bowen, A.J., 1969. Rip currents: 1. Theoretical investigations. J. Geophys. Res. 74 (23), 5467–5478. http://dx.doi.org/10.1029/JC074i023p05467.

Craciunescu, C.C., Christou, M., 2020. Wave breaking energy dissipation in long-crested focused wave groups based on JONSWAP spectra. Appl. Ocean Res. 99, 102144. http://dx.doi.org/10.1016/j.apor.2020.102144.

Cuomo, G., Allsop, W., Bruce, T., Pearson, J., 2010. Breaking wave loads at vertical seawalls and breakwaters. Coast. Eng. 57 (4), 424–439. http://dx.doi.org/10.1016/j.coastaleng.2009.11.005.

Dalrymple, R.A., Rogers, B.D., 2006. Numerical modeling of water waves with the SPH method. Coast. Eng. 53 (2–3), 141–147. http://dx.doi.org/10.1016/j.coastaleng.2005.10.004.

Dean, R.G., Dalrymple, R.A., 1991. Water Wave Mechanics for Engineers and Scientists. Vol. 2, World Scientific Publishing Company.

Deane, G.B., Stokes, D., Callaghan, A.H., 2016a. Turbulence in breaking waves. Phys. Today 69 (10), 86–87. http://dx.doi.org/10.1063/PT.3.3339.

Deane, G.B., Stokes, M.D., Callaghan, A.H., 2016b. The saturation of fluid turbulence in breaking laboratory waves and implications for whitecaps. J. Phys. Oceanogr. 46 (3), 975–992. http://dx.doi.org/10.1175/JPO-D-14-0187.1.

Deike, L., Melville, W.K., Popinet, S., 2016. Air entrainment and bubble statistics in breaking waves. J. Fluid Mech. 801, 91–129. http://dx.doi.org/10.1017/jfm.2016.372.

Derakhti, M., Kirby, J.T., Banner, M.L., Grilli, S.T., Thomson, J., 2020. A unified breaking onset criterion for surface gravity water waves in arbitrary depth. J. Geophys. Res.: Ocean. 125 (7), e2019JC015886. http://dx.doi.org/10.1029/2019JC015886.

Det Norske Veritas, 2010. DNV-RP-C205 Environmental Conditions and Environmental Loads. Technical Report, October.

Donelan, M.A., Hamilton, J., Hui, W., 1985. Directional spectra of wind-generated ocean waves. Philos. Trans. R. Soc. Lond. A 315 (1534), 509–562. http://dx.doi.org/10.1098/rsta.1985.0054.

Drazen, D.A., Melville, W.K., Lenain, L., 2008. Inertial scaling of dissipation in unsteady breaking waves. J. Fluid Mech. 611, 307–332. http://dx.doi.org/10.1017/S0022112008002826.

Ducrozet, G., Bonnefoy, F., Le Touzé, D., Ferrant, P., 2012. A modified high-order spectral method for wavemaker modeling in a numerical wave tank. Eur. J. Mech. B Fluids 34, 19–34. http://dx.doi.org/10.1016/j.euromechflu.2012.01.017.

Ducrozet, G., Bonnefoy, F., Touzé, D.L., Ferrant, P., 2016. HOS-ocean: Open-source solver for nonlinear waves in open ocean based on high-order spectral method. Comput. Phys. Comm. 203, 245–254. http://dx.doi.org/10.1016/j.cpc.2016.02.017.

Duncan, J.H., 1981. An experimental investigation of breaking waves produced by a towed hydrofoil. Proc. R. Soc. A 377 (1770), 331–348. http://dx.doi.org/10.1098/rspa.1981.0127.

Efron, B., Tibshirani, R.J., 1994. An Introduction to the Bootstrap. Chapman and Hall, CRC.

Elsayed, S.M., Gijsman, R., Schlurmann, T., Goseberg, N., 2022. Nonhydrostatic numerical modeling of fixed and mobile barred beaches: Limitations of depth-averaged wave resolving models around sandbars. J. Waterw. Port Coast. Ocean. Eng. 148 (1), 04021045. http://dx.doi.org/10.1061/(ASCE)WW.1943-5460.0000685.

Engsig-Karup, A.P., Bingham, H.B., Lindberg, O., 2009. An efficient flexible-order model for 3D nonlinear water waves. J. Comput. Phys. 228 (6), 2100–2118. http://dx.doi.org/10.1016/j.jcp.2008.11.028.

Faltinsen, O., 1990. Sea Loads on Ships and Offshore Structures. Cambridge University Press, Cambridge, UK.

Faltinsen, O.M., Landrini, M., Greco, M., 2004. Slamming in marine applications. J. Engrg. Math. 48 (3), 187–217. http://dx.doi.org/10.1023/B:engi.0000018188.68304.ae.

Fedele, F., Brennan, J., De León, S.P., Dudley, J., Dias, F., 2016. Real world ocean rogue waves explained without the modulational instability. Sci. Rep. 6, 27715. http://dx.doi.org/10.1038/srep27715.

Fedele, F., Tayfun, M.A., 2009. On nonlinear wave groups and crest statistics. J. Fluid Mech. 620, 221–239. http://dx.doi.org/10.1017/S0022112008004424.

Filipot, J.F., Ardhuin, F., Babanin, A.V., 2010. A unified deep-to-shallow water wave-breaking probability parameterization. J. Geophys. Res.: Ocean. 115 (4), 1–15. http://dx.doi.org/10.1029/2009JC005448.

Forristall, G.Z., 2000. Wave crest distributions: Observations and second-order theory. J. Phys. Oceanogr. (8), 1931–1943. http://dx.doi.org/10.1175/1520-0485(2000)030<1931:WCDOAS>2.0.CO;2.

Franco, L., de Gerloni, M., van der Meer, J., 1995. Wave overtopping on vertical and composite breakwaters. In: Coastal Engineering 1994. pp. 1030–1045. http://dx.doi.org/10.1061/9780784400890.076.

Gemmrich, J.R., Banner, M.L., Garrett, C., 2008. Spectrally resolved energy dissipation rate and momentum flux of breaking waves. J. Phys. Oceanogr. 38 (6), 1296–1312. http://dx.doi.org/10.1175/2007JPO3762.1.

Gemmrich, J.R., Farmer, D.M., 1999. Observations of the scale and occurrence of breaking surface waves. J. Phys. Oceanogr. 29 (10), 2595–2606. http://dx.doi.org/10.1175/1520-0485(1999)029<2595:OOTSAO>2.0.CO;2.

Goda, Y., 2000. Random Seas and Design of Maritime Structures. World Scientific.

Grigoriu, M., 1993. On the spectral representation method in simulation. Probab. Eng. Mech. 8 (2), 75–90. http://dx.doi.org/10.1016/0266-8920(93)90002-D.

Guedes Soares, C., Pascoal, R., 2005. On the profile of large ocean waves. J. Offshore Mech. Arct. Eng. 127 (November 2005), 306. http://dx.doi.org/10.1115/1.2087547.

Hasselmann, K., Barnett, T.P., Bouws, E., Carlson, H., Cartwright, D.E., Enke, K., Ewing, J.A., Gienapp, H., Hasselmann, D.E., Kruseman, P., Meerburg, A., Muller, P., Olbers, D.J., Richter, K., Sell, W., Walden, H., 1973. Measurements of wind-wave growth and swell decay during the joint north sea wave project (JONSWAP). Ergnzungsheft Dtsch. Hydrogr. Z. Reihe A(8) (12), 95.

Heller, V., 2017. Self-similarity and Reynolds number invariance in froude modelling. J. Hydraul. Res. 55 (3), 293–309. http://dx.doi.org/10.1080/00221686.2016.1250832.

Higuera, P., Lara, J.L., Losada, I.J., 2013. Simulating coastal engineering processes with OpenFOAM®. Coast. Eng. 71, 119–134. http://dx.doi.org/10.1016/j.coastaleng.2012.06.002.

Holthuijsen, L.H., Herbers, T.H.C., 1986. Statistics of breaking waves observed as whitecaps in the open sea. J. Phys. Oceanogr. 16 (2), 290–297. http://dx.doi.org/10.1175/1520-0485(1986)016<0290:SOBWOA>2.0.CO;2.

Hu, Z.Z., Greaves, D., Raby, A., 2016. Numerical wave tank study of extreme waves and wave-structure interaction using OpenFoam®. Ocean Eng. 126, 329–342. http://dx.doi.org/10.1016/j.oceaneng.2016.09.017.

Huang, N.E., Long, S.R., Tung, C.-C., Donelan, M.A., Yuan, Y., Lai, R.J., 1992. The local properties of ocean surface waves by the phase-time method. Geophys. Res. Lett. 19 (7), 685–688. http://dx.doi.org/10.1029/92GL00670.

Huo, C., Swan, C., Karmpadakis, I., Ma, L., 2023. An efficient method of defining the tail of a crest height distribution. Ocean Eng. 289, 116304. http://dx.doi.org/10.1016/j.oceaneng.2023.116304.

Jessup, A., Zappa, C.J., Yeh, H., 1997. Defining and quantifying microscale wave breaking with infrared imagery. J. Geophys. Res.: Ocean. 102 (C10), 23145–23153. http://dx.doi.org/10.1029/97JC01449.

Jonathan, P., Taylor, P.H., 1997. On irregular, nonlinear waves in a spread sea. J. Offshore Mech. Arct. Eng. 119 (1), 37–41. http://dx.doi.org/10.1115/1.2829043.

Karmpadakis, I., 2019. Wave Statistics in Intermediate and Shallow Water Depths (Ph.D. thesis). Imperial College London.

Karmpadakis, I., Swan, C., 2020. On the average shape of the largest waves in finite water depths. J. Phys. Oceanogr. 50 (4), 1023–1043. http://dx.doi.org/10.1175/JPO-D-19-0165.1.

Karmpadakis, I., Swan, C., 2022. A new crest height distribution for nonlinear and breaking waves in varying water depths. Ocean Eng. 266, 112972. http://dx.doi.org/10.1016/j.oceaneng.2022.112972, ID: 271462.

Karmpadakis, I., Swan, C., Christou, M., 2019. Laboratory investigation of crest height statistics in intermediate water depths. Proc. R. Soc. A: Math. Phys. Eng. Sci. 475 (2229), 20190183. http://dx.doi.org/10.1098/rspa.2019.0183.

Keeling, R.F., 1993. On the role of large bubbles in air-sea gas exchange and supersaturation in the ocean. J. Mar. Res. 51 (2), 237–271.

Kobayashi, N., Agarwal, A., Johnson, B.D., 2007. Longshore current and sediment transport on beaches. J. Waterw. Port Coast. Ocean. Eng. 133 (4), 296–304. http://dx.doi.org/10.1061/(ASCE)0733-950X(2007)133:4(296).

Kobayashi, N., Lawrence, A.R., 2004. Cross-shore sediment transport under breaking solitary waves. J. Geophys. Res.: Ocean. 109 (C3), http://dx.doi.org/10.1029/2003JC002084.

Komen, G., Hasselmann, S., Hasselmann, K., 1984. On the existence of a fully developed wind-sea spectrum. J. Phys. Oceanogr. 14, 1271–1285. http://dx.doi.org/10.1175/1520-0485(1984)014<1271:OTEOAF>2.0.CO;2.

Kway, J.H., Loh, Y.-S., Chan, E.-S., 1998. Laboratory study of deep-water breaking waves. Ocean Eng. 25 (8), 657–676. http://dx.doi.org/10.1016/S0029-8018(97)00039-5.

Lamarre, E., Melville, W.K., 1994. Void-fraction measurements and sound-speed fields in bubble plumes generated by breaking waves. J. Acoust. Soc. Am. 95 (3), 1317–1328. http://dx.doi.org/10.1121/1.408572.

Latheef, M., Swan, C., 2013. A laboratory study of wave crest statistics and the role of directional spreading. Proc. R. Soc. A: Math. Phys. Eng. Sci. 469 (2152), 20120696. http://dx.doi.org/10.1098/rspa.2012.0696.

Latheef, M., Swan, C., Spinneken, J., 2017. A laboratory study of nonlinear changes in the directionality of extreme seas. Proc. R. Soc. A 473 (2199), 20160290. http://dx.doi.org/10.1098/rspa.2016.0290.

Le Méhauté, B., 1962. On non-saturated breakers and the wave run-up. In: Proceedings of the 8th International Conference on Coastal Engineering. pp. 77–92. http://dx.doi.org/10.9753/icce.v8.6.

Li, Y., Larsen, B.E., Fuhrman, D.R., 2022. Reynolds stress turbulence modelling of surf zone breaking waves. J. Fluid Mech. 937, 1–44. http://dx.doi.org/10.1017/jfm.2022.92.

Liberzon, D., Vreme, A., Knobler, S., Bentwich, I., 2019. Detection of breaking waves in single wave gauge records of surface elevation fluctuations. J. Atmos. Ocean. Technol. 36 (9), 1863–1879. http://dx.doi.org/10.1175/JTECH-D-19-0011.1.

Liu, S., Wang, H., Bayeul-Lainé, A.-C., Li, C., Katz, J., Coutier-Delgosha, O., 2023. Wave statistics and energy dissipation of shallow-water breaking waves in a tank with a level bottom. J. Fluid Mech. 975, A25. http://dx.doi.org/10.1017/jfm.2023.876.

Longuet-Higgins, M.S., 1952. On the statistical distribution of sea waves. J. Mar. Res. 11, 245–266.

Longuet-Higgins, M.S., 1969. A nonlinear mechanism for the generation of sea waves. Proc. R. Soc. A 311 (1506), 371–389. http://dx.doi.org/10.1098/rspa.1969.0123.

Longuet-Higgins, M.S., 1970. Longshore currents generated by obliquely incident sea waves: 1. J. Geophys. Res. 75 (33), 6778–6789. http://dx.doi.org/10.1029/JC075i033p06778.

Longuet-Higgins, M.S., 1982. On the skewness of sea-surface slopes. J. Phys. Oceanogr. 12 (11), 1283–1291. http://dx.doi.org/10.1175/1520-0485(1982)012<1283:OTSOSS>2.0.CO;2.

Longuet-Higgins, M.S., Stewart, R.W., 1960. Changes in the form of short gravity waves on long waves and tidal currents. J. Fluid Mech. 8 (4), 565–583. http://dx.doi.org/10.1017/S0022112060000803.

Longuet-Higgins, M.S., Stewart, R., 1964. Radiation stresses in water waves; a physical discussion, with applications. Deep. Sea Res. Ocean. Abstr. 11 (4), 529–562. http://dx.doi.org/10.1016/0011-7471(64)90001-4, ID: 272880.

Ma, L., Swan, C., 2020. An experimental study of wave-in-deck loading and its dependence on the properties of the incident waves. J. Fluids Struct. 92, 102784. http://dx.doi.org/10.1016/j.jfluidstructs.2019.102784.

Martins, K., Blenkinsopp, C.E., Power, H.E., Bruder, B., Puleo, J.A., Bergsma, E.W., 2017. High-resolution monitoring of wave transformation in the surf zone using a LiDAR scanner array. Coast. Eng. 128, 37–43. http://dx.doi.org/10.1016/j.coastaleng.2017.07.007.

Masterton, S.R., Swan, C., 2008. On the accurate and efficient calibration of a 3D wave basin. Ocean Eng. 35, 763–773. http://dx.doi.org/10.1016/j.oceaneng.2008.02.002.

McAllister, M.L., Pizzo, N., Draycott, S., Bremer, T.S.V.D., 2023. The influence of spectral bandwidth and shape on deep-water wave breaking onset. J. Fluid Mech. 974, A14. http://dx.doi.org/10.1017/jfm.2023.766.

van der Meer, J., Akbar, R., Mukhdiar, R., Briganti, R., Musumeci, R.E., Romano, A., Suzuki, T., Altomare, C., 2018. Wave overtopping with a changing steep sandy foreshore, conventional and numerical analysis of results. Coast. Eng. Proc. (36), http://dx.doi.org/10.9753/icce.v36.waves.65, 65–65.

Melville, W.K., Matusov, P., 2002. Distribution of breaking waves at the ocean surface. Nature 417 (6884), 58–63. http://dx.doi.org/10.1038/417058a.

Miche, R., 1944. Mouvements ondulatoires de lamer en profondeur ou décroissante. Ann. Ponts Chaussées 19, 370–406.

Mostert, W., Popinet, S., Deike, L., 2022. High-resolution direct simulation of deep water breaking waves: transition to turbulence, bubbles and droplets production. J. Fluid Mech. 942, A27. http://dx.doi.org/10.1017/jfm.2022.330.

Munk, W.H., 1949. The solitary wave theory and its application to surf problems. Ann. New York Acad. Sci. 51 (3), 376–424. http://dx.doi.org/10.1111/j.1749-6632.1949.tb27281.x.

Pierson, W.J., Moskowitz, L., 1964. A proposed spectral form for fully developed wind seas based on the similarity theory of S. A. Kitaigorodskii. J. Geophys. Res. 69 (24), 5181–5190. http://dx.doi.org/10.1029/JZ069i024p05181.

Prevosto, M., Krogstad, H.E., Robin, A., 2000. Probability distributions for maximum wave and crest heights. Coast. Eng. 40 (4), 329–360. http://dx.doi.org/10.1016/S0378-3839(00)00017-X.

Pullen, T., Allsop, W., Bruce, T., Pearson, J., 2009. Field and laboratory measurements of mean overtopping discharges and spatial distributions at vertical seawalls. Coast. Eng. 56 (2), 121–140. http://dx.doi.org/10.1016/j.coastaleng.2008.03.011.

Raby, A., 2003. Extreme Waves, Overtopping and Flooding at Sea Defences (Ph.D. thesis). University of Oxford.

Rapp, R.J., Melville, W.K., 1990. Laboratory measurements of deep-water breaking waves. Philos. Trans. R. Soc. A: Math. Phys. Eng. Sci. A 331, 735–800. http://dx.doi.org/10.1098/rsta.1990.0098.

Schwendeman, M.S., Thomson, J., 2017. Sharp-crested breaking surface waves observed from a ship-based stereo video system. J. Phys. Oceanogr. 47 (4), 775–792. http://dx.doi.org/10.1175/JPO-D-16-0187.1.

Schwendeman, M., Thomson, J., Gemmrich, J.R., 2014. Wave breaking dissipation in a young wind sea. J. Phys. Oceanogr. 44 (1), 104–127. http://dx.doi.org/10.1175/JPO-D-12-0237.1.

Seiffert, B.R., Ducrozet, G., 2018. Simulation of breaking waves using the high-order spectral method with laboratory experiments: wave-breaking energy dissipation. Ocean. Dyn. 68 (1), 65–89. http://dx.doi.org/10.1007/s10236-017-1119-3.

Seiffert, B.R., Ducrozet, G., Bonnefoy, F., 2017. Simulation of breaking waves using the high-order spectral method with laboratory experiments: Wave-breaking onset. Ocean. Model. 119, 94–104. http://dx.doi.org/10.1016/j.ocemod.2017.09.006.

Sharma, N., Dean, R., 1981. Second-order directional seas and associated wave forces. Soc. Pet. Eng. J. 21 (1), 129–140. http://dx.doi.org/10.2118/8584-PA.

Shi, F., Kirby, J.T., Harris, J.C., Geiman, J.D., Grilli, S.T., 2012. A high-order adaptive time-stepping TVD solver for Boussinesq modeling of breaking waves and coastal inundation. Ocean. Model. 43, 36–51. http://dx.doi.org/10.1016/j.ocemod.2011.12.004.

Socquet-Juglard, H., Dysthe, K.B., Trulsen, K., Krogstad, H.E., Liu, J., 2005. Probability distributions of surface gravity waves during spectral changes. J. Fluid Mech. 542 (2005), 195–216. http://dx.doi.org/10.1017/S0022112005006312.

Spiliotopoulos, G., Katsardi, V., 2024. Effects of nonlinearity on the crest shape of extreme irregular sea waves: Nonlinear harmonic separation and analysis. Phys. Fluids 36 (10), http://dx.doi.org/10.1063/5.0229953.

Spinneken, J., Swan, C., 2012. The operation of a 3D wave basin in force control. Ocean Eng. 88–100. http://dx.doi.org/10.1016/j.oceaneng.2012.07.024.

Srokosz, M., Longuet-Higgins, M., 1986. On the skewness of sea-surface elevation. J. Fluid Mech. 164, 487–497. http://dx.doi.org/10.1017/S0022112086002653.

Stansberg, C.T., Berget, K., Graczyk, M., Muthanna, C., Pakozdi, C., 2012. Breaking wave kinematics and resulting slamming pressures on a vertical column. In: International Conference on Offshore Mechanics and Arctic Engineering. Vol. 44885, American Society of Mechanical Engineers, pp. 679–689. http://dx.doi.org/10.1115/OMAE2012-83929.

Stansby, P.K., Devaney, L.C., Stallard, T.J., 2013. Breaking wave loads on monopiles for offshore wind turbines and estimation of extreme overturning moment. IET Renew. Power Gener. 7 (5), 514–520. http://dx.doi.org/10.1049/iet-rpg.2012.0205.

Stansell, P., MacFarlane, C., 2002. Experimental investigation of wave breaking criteria based on wave phase speeds. J. Phys. Oceanogr. 32 (5), 1269–1283. http://dx.doi.org/10.1175/1520-0485(2002)032<1269:EIOWBC>2.0.CO;2.

Su, M.-Y., Cartmill, J., 1991. Breaking wave statistics obtained during 'swade'. In: Breaking Waves: IUTAM Symposium Sydney, Australia 1991. Springer, pp. 161–164.

Sutherland, P., Melville, W.K., 2013. Field measurements and scaling of ocean surface wave-breaking statistics. Geophys. Res. Lett. 40 (12), 3074–3079. http://dx.doi.org/10.1002/grl.50584.

Tang, T., Moss, C., Draycott, S., Bingham, H.B., Van Den Bremer, T.S., Li, Y., Adcock, T.A., 2023. The influence of directional spreading on rogue waves triggered by abrupt depth transitions. J. Fluid Mech. 972, R2. http://dx.doi.org/10.1017/jfm.2023.737.

Tayfun, M.A., 1980. Narrow-band nonlinear sea waves. J. Geophys. Res. (C3), 1548. http://dx.doi.org/10.1029/JC085iC03p01548.

Tayfun, M.A., 1981. Distribution of crest-to-trough wave heights. J. Waterw. Port Coast. Ocean. Eng. 107 (WW3), 149–158. http://dx.doi.org/10.1061/JWPCDX.0000259.

Tayfun, M.A., 2006. Statistics of nonlinear wave crests and groups. Ocean Eng. 33 (11–12), 1589–1622. http://dx.doi.org/10.1016/j.oceaneng.2005.10.007.

Tayfun, M.A., Fedele, F., 2007. Wave-height distributions and nonlinear effects. Ocean Eng. 34 (11–12), 1631–1649. http://dx.doi.org/10.1016/j.oceaneng.2006.11.006.

Thornton, E.B., Guza, R.T., 1983. Transformation of wave height distribution. J. Geophys. Res. (C10), 5925. http://dx.doi.org/10.1029/JC088iC10p05925.

Tian, Z., Perlin, M., Choi, W., 2012. An eddy viscosity model for two-dimensional breaking waves and its validation with laboratory experiments. Phys. Fluids 24 (3), http://dx.doi.org/10.1063/1.3687508.

Tucker, M.J., Pitt, E.G., 2001. Waves in Ocean Engineering. p. 550. http://dx.doi.org/10.1016/0141-0296(92)90048-U.

Wang, Y., Ducrozet, G., 2025. Computing local crest phase speed in multi-directional sea states through the spatial Hilbert transform. Ocean Eng. 331, 121357. http://dx.doi.org/10.1016/j.oceaneng.2025.121357.

Weissman, M., Ataktürk, S., Katsaros, K., 1984. Detection of breaking events in a wind-generated wave field. J. Phys. Oceanogr. 14 (10), 1608–1619. http://dx.doi.org/10.1175/1520-0485(1984)014<1608:DOBEIA>2.0.CO;2.

Wu, C.H., Nepf, H.M., 2002. Breaking criteria and energy losses for three-dimensional wave breaking. J. Geophys. Res. (C10), 3177. http://dx.doi.org/10.1029/2001JC001077.

Young, I., Banner, M., 1992. Numerical experiments on the evolution of fetch limited waves. In: Breaking Waves: IUTAM Symposium Sydney, Australia 1991. Springer, pp. 267–275.

Zappa, C.J., Asher, W.E., Jessup, A.T., 2001. Microscale wave breaking and air-water gas transfer. J. Geophys. Res.: Ocean. 106 (C5), 9385–9391. http://dx.doi.org/10.1029/2000JC000262.

Zijlema, M., Stelling, G., Smit, P., 2011. SWASH: An operational public domain code for simulating wave fields and rapidly varied flows in coastal waters. Coast. Eng. 58 (10), 992–1012. http://dx.doi.org/10.1016/j.coastaleng.2011.05.015.